Eidgenössische Technische Hochschule Zürich
Swiss Federal Institute of Technology Zurich

Empa
Materials Science and Technology

Deformation Analysis and Finite Element Modelling for Ti-6Al-4V Additive Manufactured Lattices

Master Thesis

Serjosha Robmann

August 30, 2019

Advisors: Prof. Dr. E. Mazza, Dr. E. Hosseini

306 - Experimental Continuum Mechanics, Empa

Abstract

Additive manufacturing is a promising production process with unique benefits in various fields. Due to the high investment costs and the currently slow build rates it is only used and considered presently in highly specific applications. For example the realization of complex geometries as cellular structures with selective laser melting (SLM). Such structures offer several advantages, as an adaptable compliance, which is important for orthopaedic implants to prevent stress shielding. A fundamental drawback is the uncertainty of the mechanical integrity of the manufactured parts and additional research is necessary for a future implementation.

As part of this thesis tensile tests were conducted on single strut samples (diameter and length of 200 µm and 2 mm) printed with different orientations to determine the anisotropic behavior of SLM Ti-6Al-4V. Samples with five varying orientations reaching from horizontal (parallel to printing plane) to vertical (perpendicular to printing plane) were printed and examined. Digital image correlation (DIC) was used for monitoring strain development in the strut specimens. A geometrical analysis of the samples highlighted the large mismatches between the nominal and actual geometry of the printed samples. Derivation of a material model from the experimental observations therefore was based on the actual geometry of the samples. A finite element (FE) based optimization methodology employed the μCT reconstructed geometries of the specimens and derived a reliable material model for SLM Ti-6Al-4V. Tension, compression and shear tests were performed for SLM Ti-6Al-4V lattice structures to be employed for effectiveness demonstration of the derived material model.

Detailed examinations showed that the FE models based on the μCT data and the material model derived from the strut specimens can well represent the deformation behavior of lattice specimens under tension and compression loading, but fails for prediction of their behavior under shear deformation. Nevertheless, the FE predicted strain distributions for all the loading conditions were comparable with those recorded by DIC for lattices. Further investigations are necessary to fully understand the deviation of the FE model and the experimental results for the shear behavior.

Acknowledgements

I would like to thank Prof. Dr. Edoardo Mazza for the chance to write my master thesis in the Experimental Continuum Mechanics laboratory and for supporting me as tutor during my master's degree. A special thanks goes to Dr. Ehsan Hosseini, who continuously advised me during the last six months with an enormous cooperativeness. I am grateful for the interesting discussions and challenges of the last six months and the research I was able to conduct.

Additionally many thanks goes to all the other people in the Experimental Continuum Mechanics laboratory. Not only for their support in many applications as the microscope and scanning electron microscope (SEM) sessions but also for their welcoming and supportive way. Their aid with ambiguity and interesting discussions were highly helpful.

Last but not least I would like to thank my family and Anna for their support during these six months.

Contents

List of Figures

List of Tables

Chapter 1

Introduction

1.1 Motivation

Additive Manufacturing (AM) is a relatively new production technology with numerous promising new features, which are discussed in detail in section 1.2. Due to its characteristics, additive manufacturing is especially interesting for highly specific applications in the field of aerospace/space or biomedical engineering. Advantages like the huge freedom of design or the possibility to produce lightweight parts qualifies the technology for the fabrication of functionally integrated parts. A possible application could be a rocket motor with integrated cooling channels in the wall of the burning chamber and nozzle. But also highly complex parts as for example fuel injection nozzles for turbines could be additively manufactured.

Another interesting advantage is the possibility to build cellular and functionally graded structures. These structures have a defined porosity and specific stiffness behavior. These properties predestine the additive manufacturing for the fabrication of medical implants. Due to the porosity the possibility for bone ingrowth is given. The fact that the stiffness behavior can be modified by the unit cell design provides the possibility to tune the stiffness of the structure to the medium's specific material behavior, which would decrease the risk for stress shielding in orthopedic implants.

Due to the particular production process, which can be compared to a welding process, the material properties of AM materials differ partially significantly from the conventionally manufactured materials. Numerous ongoing researches try to describe the material properties of AM materials. They report an anisotropic material behavior with often inferior material properties. Most of these studies focused on relatively large AM samples to obtain the material parameters. For applications with thin material sections, e.g.

cellular structures, it is probably more reasonable to extract the material properties from miniature specimens with thin cross-sections.

The basic information about additive manufacturing can be found in the introduction section, which is gathering the most relevant aspects for the topic of this thesis. The methods section is explaining the experimental setups and describing the available samples used for testing. The experimental results section is presenting the results obtained of the experimental part and is then highlighting the difficulties faced during the examination of the samples. The performed FE simulations and their goals are discussed in the simulation section and the performance of the material model is presented at the end of this section. The conclusion and outlook section includes the most important results and observations and presents further possible research based on the found results and conclusions.

1.2 Additive Manufacturing

Additive manufacturing (AM) is a general description of the process of adding material layer by layer to produce a part instead of subtracting parts from a bulk piece of material, which is still the most used process nowadays. Additive manufacturing includes numerous processes for various materials. For plastic materials the most common ones are fused deposition modelling (FDM) and selective laser sintering (SLS). For metals the most common additive manufacturing methods are the powder bed fusion process, including selective laser melting (SLM) and electron beam melting (EBM), and directed energy deposition (DED). All of these processes offer different advantages and limitations, which predestine them for a certain application. We will focus on the SLM process, the presently most used metal additive manufacturing process, and which was used to produce our test samples. Various materials exist for the SLM process: steel (316L), copper, aluminum alloy (AlSi12) and titanium alloy (Ti-6Al-4V). For our samples Ti-6Al-4V was used, the most common $\alpha + \beta$ titanium alloy which stands out for its high strength, low density and good corrosion resistance. The good biocompatibility and the low elastic modulus qualifies it for the use in biomedical applications. Ti-6Al-4V is also especially interesting for the AM application due to its poor thermal conductivity and the active chemical reactivity to oxygen, which makes it difficult and expensive to machine [11].

1.2.1 Applications

Due to its characteristics additive manufacturing is used for highly specific applications mainly in the following areas:

- Aerospace/space
- Automotive
- Medical
- Prototyping

The main reasons why additive manufacturing is used in highly specific applications is because of the advantages and disadvantages of the manufacturing process (see [5]).

Advantages	Disadvantages
- Freedom of design	- High investment costs
- Lightweight design	- Slow build rates
- Cellular and functionally graded structures	- Uncertainties regarding material properties
- Multi-material parts	- Post-processing necessary
- Smaller environmental footprint	- Limited choice of material and component size

To better understand the reasons for the above mentioned points, a short overview of the SLM process is helpful. For this reason the process and the resulting material properties are shortly discussed in section 1.2.2 and 1.2.3 respectively.

1.2.2 Process Description

To comprehend the challenges of SLM, it is necessary to understand the process and its characteristics. This section will describe the SLM process, figure 1.1 is giving a rough overview of the most important components, and the main reasons for the obtained material properties. SLM emerged in the last two decades and is the most common metal additive manufacturing process today. The process builds up a part by successively melting layers of powder. The melting is done by one or even more laser beams. The parts are manufactured on the build platform, which is lowered for every layer by the preset layer thickness. The new powder layer is applied by a

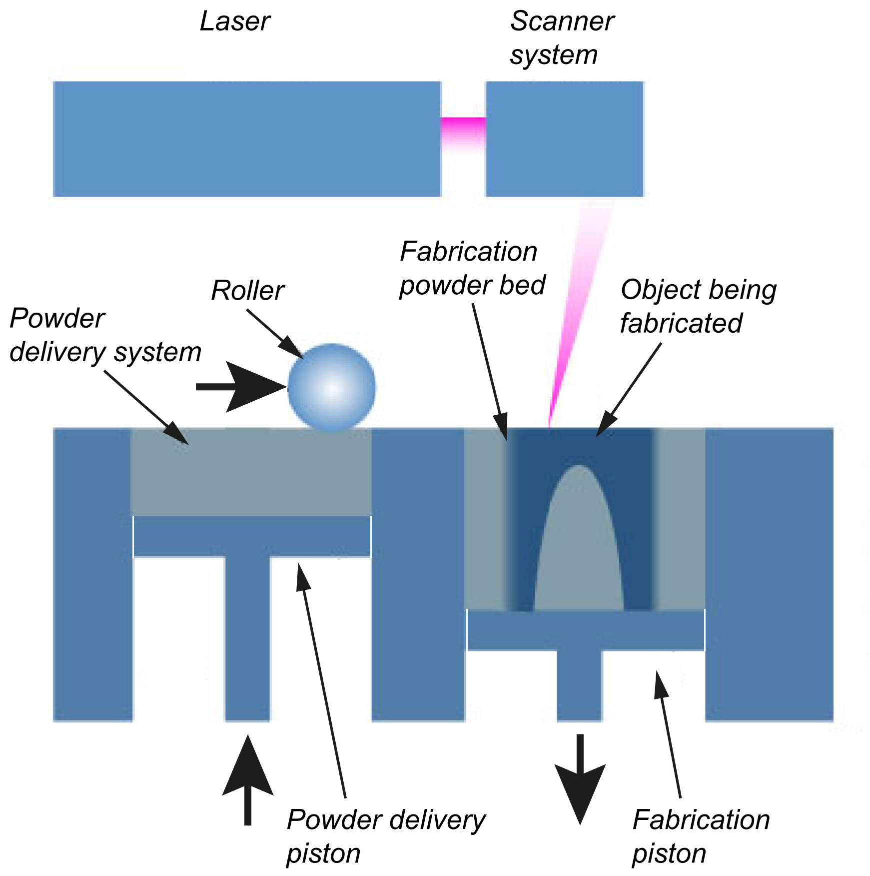

Figure 1.1: Simplified process SLM process overview with the most important elements [5].

roller, which is distributing the powder homogeneously on the build platform. The unmelted powder remains on the build platform until the end of the manufacturing process and serves as a support for the parts. Additional solid type support structure might be needed for the part to withstand the large residual stresses induced by the large temperature gradients during the printing process [11].

At the end of the manufacturing process the powder will be removed manually, and various heat treatments are applied to reduce the residual stresses. For example annealing or hot isostatic pressing (HIP), which is trying to increase the density of the printed parts by closing internal pores. These pores are process induced and are highly process parameter dependent. Although with optimal process parameters, a density of almost 100 % can be achieved the existing AM induced pores can affect the material's mechanical response considerably. With HIP the density can be further improved and therefore improve the mechanical integrity of the parts (see [11]). After the heat treatment, the parts are mechanically removed from the build platform and the final post-processing (e.g. surface finishing) can be done.

1.2.3 Material Properties

With the process description in section 1.2.2 in mind, it is possible to understand the reason for the anisotropic behavior of the manufactured parts. During the SLM process the laser is remelting the previous layers and therefore allows for formation of elongated grains parallel to the printing direction which share a similar crystallographic orientation. The other parameter which contributes to anisotropic property is the layer wise production process which affect the distribution of AM induced pores and also result in different surface roughness in directions parallel and perpendicular to the printing plane. This elongated grains cause the anisotropic behavior of the additively manufactured Ti-6Al-4V samples. For Ti-6Al-4V, the samples show a higher elongation with decreased stiffness and strength parallel to the printing direction and a decreased elongation with higher stiffness and strength parallel to the printing plane (see [8]). Other studies reported a similar behavior for the elongation of the samples but reported a different behavior for the ultimate strength (see [1]). The comparison of different studies shows a large variation of the anisotropic behavior, which indicates that other effects also have to be considered. For example [11] reported for as-built SLM parts an ultimate tensile strength reaching from 1000 MPa to over 1400 MPa.

The typical microstructure of additively manufactured Ti-6Al-4V is consisting of martensitic α' within columnar β grain (see [8]). In general the detailed phase distribution is highly temperature history dependent and can change even with the layer height within the sample (see [7]). Due to the temperature dependent phase distribution, the material properties can vary significantly between different builds or even within a single build. For example [7] reported an elastic modulus of (166.6 ± 5.1) GPa for the martensitic phase, which is significantly higher than the approximately expected 120 GPa for Ti-6Al-4V. For this reason a metallurgical analysis of the printed samples might be helpful to fully understand their material properties.

1.2.4 Lattice structures

The term lattice structure describes a geometry which is formed by periodically arranging the so called unit cells. They are often associated with cellular solids, which is also shown in figure 1.2. They possess several advantages to conventional structures, they have often a superior stiffness-to-weight-ratio and it is possible to easily tune their stiffness behavior. Due to the small scale unit cell, it can be handled as monolithic material with its own material properties. This allows us to highly modify the overall behavior of the structure by redesigning our unit cell [12].

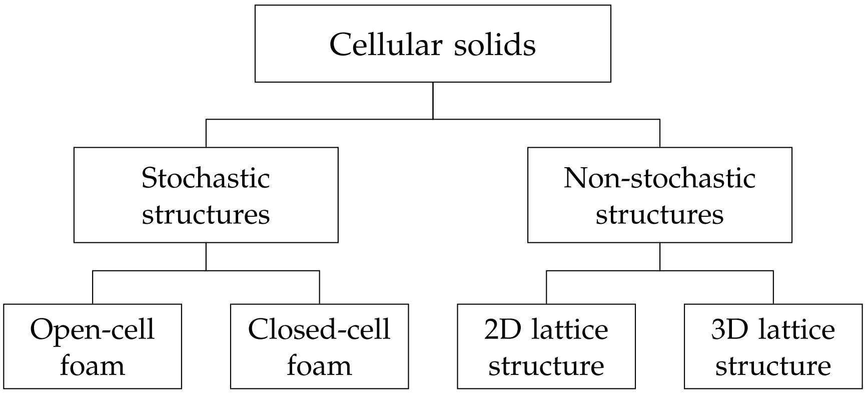

Figure 1.2: Categories of cellular structures according to [12].

The unit cell of lattice structures are either bend or stretch dominated. This means the unit cell deforms either by bending the struts or by mainly stretching/compressing the struts. The bending dominated lattices would actually behave like a mechanism if we would assume frictionless joints, whereas the stretch dominated would still carry all the load. The main advantage of a stretch dominated unit cell is the increased stiffness-to-weight-ratio. As an example, the stretch dominated unit cell examined in [6] were ten times stiffer and three times stronger than a bending dominated one. To determine if the unit cell is bend or stretch oriented one can use the Maxwell's criterion for a 2D (eq. 1.1) and 3D (eq. 1.2) frame [6]:

$$b - 2j = s - m \tag{1.1}$$

$$b - 3j + 6 = s - m \tag{1.2}$$

where b is the number of struts and j is the number of joints. Whereas s describes the states of self stress and m the number of mechanisms.

1.2.5 Geometry-mismatch compensation

The geometries of lattice structures are in the microscale and for various application a size as small as possible is preferred. Unfortunately current additive manufacturing technologies are producing large geometrical mismatches, which increase for smaller architectures. In other words, the accuracy and reproducibility for smaller geometries decreases. This is due to the smallest possible resolution of the manufacturing process. These discrepancies can significantly affect the overall performance of the lattice structure. Not only the interplay with the biological medium, due to its changed porosity, but also the expected mechanical property would be affected due to the mentioned mismatches. The most affected geometrical features are the strut thickness, strut cross-section, strut straightness and pore size (see [10]). For this reason different methods are suggested to compensate the manufacturing process induced mismatches, which can be classified in three groups: design-oriented, process-control and post-processing strategies. The design-oriented approach tries to compensate manufacturing differences by adapting the nominal geometry, whereas the process-control strategy tries to influence the final result by tuning the manufacturing machine parameters. The post-processing strategy tries to optimize the result by further process tooling the printed product for example with electro polishing (see [10]).

For our samples, the design-oriented approach was used. They analyzed the unit cells of printed lattice structures and compared them to the nominal geometry. A significant oversizing for the horizontal struts and a decreased overmelting for the vertical struts was observed - which in their case even resulted in undersized vertical struts. Their approach is based on a comparison of nominal to printed geometry. A spider-web with different angles was printed and used to establish a correlation between the nominal and the printed part. This correlation was then used to compensate the nominal geometry so that the printed geometry would have the expected dimensions. Their method showed promising results and they lowered the horizontal mismatch from 60 % to 3.1 % (see [10]). Based on these results, the same compensation method was used to produce our samples.

1.3 Medical Application

1.3.1 Bone Ingrowth and Porosity

During the 1950's, the joint replacement was conducted with the use of cement. It was a revolutionary step for the field of orthopaedic surgery and the method was improved and applied to various joints. In the 1980's, first studies appeared showing the drawback of using cement. Due to stress shielding (see 1.3.2) the bone started to reduce density which led to loosening of the implant [2]. These failures increased the interest for a cementless fixation of the implants, a method to permanently fix an implant without any additional phase. One possibility to fix an implant for longterm usage is using the bone ingrowth - also called osseointegration. A successful longterm fixation depends on a good and quick osseointegration. One of the important factors for a fast bone ingrowth is the porosity of the cellular structure.

According to [10] the porosity φ is defined as

$$\varphi(\%) = (1 - \frac{V_P}{V_S}) \times 100 \tag{1.3}$$

where V_P is the volume of empty space in the geometry and V_S includes the total volume of the geometry. It describes the void of a structure in percentage, in other words, how many percentage of the volume are not filled with material. The porosity is especially important, as it not only allows osseointegration, but also reduces the stiffness of the implants.

1.3.2 Stress Shielding

Stress shielding is describing the effect of bone absorption after a partial or complete implantation of e.g. the hip. The explanation for the behavior of the bone can be found in Wolff's law. This law states that the bone of a healthy person or animal will always adapt to the applied loads [2]. For example weightlifters show an increased bone density caused by their training. On the other hand, the bone density is decreasing if the loads are decreased. Astronauts show decreased bone density after a long stay in space, due to the decreased gravitational forces. A similar behavior can be observed for bone around implants. Due to the implant's increased stiffness, the bone is experiencing a significant reduction in its force, which then leads to a reduced bone density around the implant, also known as stress shielding. This shows the significant advantage offered by the use of cellular or lattice structures for fabrication of implants. Due to the possibility to tune their stiffness behavior the stress shielding can be minimized. The stiffness behavior can be modified to a comparable scale as the cortical bone stiffness of 3 GPa - 30 GPa (see [13]), where the Femur is around 17 GPa, or the cancellous bone stiffness of 0.04 GPa - 1.0 GPa (see [2]). The cortical bone is the hard outer layer of a bone, whereas the cancellous (trabecular) bone is the spongy part of the bone and is typically found at the ends of long bones.

Figure 1.3: X-ray picture of a hip implant. The stress shielding can clearly be seen by the darkened (low density) bone region around the implant.

1.4 Linear Elasticity

1.4.1 Isotropic Modelling

This section will discuss the constitutive modelling of the linear elastic region and its implementation for ABAQUS. It begins with the uniaxial definition, which is also used to determine the stress-strain curves of our strut samples. The uniaxial definition will then be generalized to the three dimensional state and the implementation in ABAQUS will be discussed. If not cited differently all the information in this section are taken from the ABAQUS Documentation [3].

The uniaxial linear elastic material behavior can be defined as

$$\sigma = E\varepsilon \tag{1.4}$$

Where σ is the stress, ε is the elastic strain and E is the elastic modulus. With this equation, we can determine the elastic modulus of our samples from the tensile tests. This formulation is adequate for a uniaxial tensile test. To define an isotropic elastic material model in ABAQUS, the Poisson's ration is additionally needed. An isotropic material model was used within the first iteration of the optimization to check if there exist an apparent anisotropy. The isotropic material model is implemented by ABAQUS using the fourth order elasticity tensor D:

$$\sigma_{ij} = D_{ijkl}\varepsilon_{kl} \tag{1.5}$$

using the Voigt-notation the elasticity tensor looks as follows for our isotropic material model:

$$\sigma = \begin{bmatrix} \frac{1}{E} & \frac{-\nu}{E} & \frac{-\nu}{E} & 0 & 0 & 0 \\ \frac{-\nu}{E} & \frac{1}{E} & \frac{-\nu}{E} & 0 & 0 & 0 \\ \frac{-\nu}{E} & \frac{-\nu}{E} & \frac{1}{E} & 0 & 0 & 0 \\ 0 & 0 & 0 & \frac{1}{G} & 0 & 0 \\ 0 & 0 & 0 & 0 & \frac{1}{G} & 0 \\ 0 & 0 & 0 & 0 & 0 & \frac{1}{G} \end{bmatrix} \varepsilon \tag{1.6}$$

With

$$G = \frac{E}{2(1+\nu})) \tag{1.7}$$

Accordingly, the stress tensor can be written as (see [4]):

$$\sigma_{ij} = \frac{E}{1+\nu}[\varepsilon_{ij} + \frac{\nu}{1-2\nu}\varepsilon_{kk}\delta_{ij}] \tag{1.8}$$

1.4.2 Anisotropic Modelling

The fourth order elasticity tensor D consists of 21 independent parameters, this is due to symmetry of the stress and the strain tensor. Assuming orthogonal symmetries and using x_1, x_2 and x_3 as principal axes reduce the 21 parameters to nine. The relationship between stress and strain tensor are:

$$\sigma = \begin{bmatrix} \frac{1}{E_1} & -\frac{\nu_{21}}{E_2} & -\frac{\nu_{31}}{E_3} & 0 & 0 & 0 \\ -\frac{\nu_{12}}{E_1} & \frac{1}{E_2} & -\frac{\nu_{32}}{E_3} & 0 & 0 & 0 \\ -\frac{\nu_{13}}{E_1} & -\frac{\nu_{23}}{E_2} & \frac{1}{E_3} & 0 & 0 & 0 \\ 0 & 0 & 0 & \frac{1}{G_{12}} & 0 & 0 \\ 0 & 0 & 0 & 0 & \frac{1}{G_{13}} & 0 \\ 0 & 0 & 0 & 0 & 0 & \frac{1}{G_{23}} \end{bmatrix} \varepsilon \tag{1.9}$$

To implement an orthotropic material model in ABAQUS, the engineering constants are the most intuitive ones. The engineering constants for a fully orthotropic material are the three elastic moduli: E_1, E_2 and E_3, the three Poisson's ratios: ν_{12}, ν_{13} and ν_{23} and the three shear moduli: G_1, G_2 and G_3.

For the implemented material model we assume symmetry for the printing plane, which is not suitable for every case and depends on the scanning strategy. This is called transversally isotropic, similar to metals formed by deep drawing. Again the engineering constants are the easiest solution to define such a material model. The elasticity tensor will look as follows for a transversally isotropic material:

$$\sigma = \begin{bmatrix} \frac{1}{E_p} & -\frac{\nu_p}{E_p} & -\frac{\nu_{tp}}{E_t} & 0 & 0 & 0 \\ -\frac{\nu_p}{E_p} & \frac{1}{E_p} & -\frac{\nu_{tp}}{E_t} & 0 & 0 & 0 \\ -\frac{\nu_{pt}}{E_p} & -\frac{\nu_{pt}}{E_p} & \frac{1}{E_t} & 0 & 0 & 0 \\ 0 & 0 & 0 & \frac{1}{G_p} & 0 & 0 \\ 0 & 0 & 0 & 0 & \frac{1}{G_t} & 0 \\ 0 & 0 & 0 & 0 & 0 & \frac{1}{G_t} \end{bmatrix} \varepsilon \tag{1.10}$$

Where the following conditions are used $E_p = E_1 = E_2$, $E_t = E_3$, $\nu_p = \nu_1 = \nu_2$, $G_p = G_1$ and $G_t = G_2 = G_3$. If we take into account that

$$G_p = \frac{E_p}{2(1+\nu_p)} \tag{1.11}$$

only five independent constants are left to define: E_p, E_t, ν_p, ν_{tp} and G_t. To define the transversally isotropic material model in ABAQUS the above mentioned relations have to be used to define the nine required engineering constants.

1.5 Plasticity

Plasticity can be defined in ABAQUS with various possibilities. Unfortunately many of them are only available in ABAQUS Explicit, especially if an anisotropic yielding has to be implemented. For this setup, the only possibility in ABAQUS Standard is the definition of the plasticity and strain hardening with tabular data. The input data was generated by a script, which is using the Armstrong-Frederick model.

1.5.1 Yield Surface

The most common yield criterion is the von Mises yield criterion. The definition based on principal values is (see [4]):

$$\sigma_{Mises} = \sqrt{\sigma_1^2 + \sigma_2^2 + \sigma_3^3 - \sigma_1\sigma_2 - \sigma_2\sigma_3 - \sigma_3\sigma_1} \tag{1.12}$$

To define anisotropic yielding the Hill's potential function can be used, which is a modified von Mises criterion:

$$\sigma_{Hill} = \sqrt{F(\sigma_2-\sigma_3)^2 + G(\sigma_3-\sigma_1)^2 + H(\sigma_1-\sigma_2)^2 + 2L\sigma_{23}^2 + 2M\sigma_{31}^2 + 2N\sigma_{12}^2} \tag{1.13}$$

Where F,G, H, L, M and N are constants defining the level of anisotropy. In ABAQUS, the Hill's potential function can be used to define the anisotropic yield behavior. For this purpose as suboption for the plasitc behavior a potential has to be defined, which is consisting of six ratios R_{ij}. These yield ratios define the corresponding yield stress for each stress component as $R_{ij}\sigma$ where σ is the stress value defined for the plastic behavior. The yield ratios are defined accordingly to the transversally isotropic elasticity (see 1.4.2).

1.5.2 Hardening

Because an implicit solution would be preferred and ABAQUS explicit is avoided, the choice of anisotropic yield model limits the possibilities for hardening definition to the use of tabular data. For this reason the tabular data for the plasticity definition was defined with a function implemented in a Matlab script. The Armstrong-Frederick model was used for this purpose, which is a exponential hardening function based on the Chaboche model:

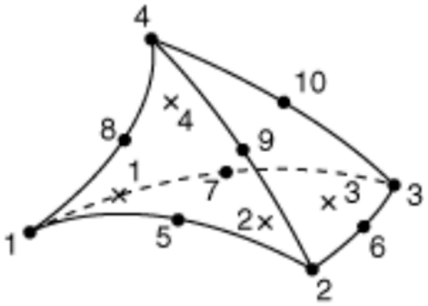

Figure 1.4: Node (bullet points) numbering of the C3D10 element with the four integration points (crosses).

$$\sigma = \sigma_0 + \frac{C}{\gamma}(1 - \exp(-\gamma \varepsilon_p)) \tag{1.14}$$

The equation is defining the stress σ as a function of the yield stress σ_0 and the exponential hardening function, defined by the strain hardening parameter C and the strain softening parameter γ. To improve the hardening behavior description a sum of several exponential hardening functions, for our material model two terms were implemented, might be used.

1.6 Element Types

The most common element to mesh irregular shaped geometries, as we obtain from our CT data, is the tetrahedral element, which are also available in the software packages used to mesh the CT data. The user can switch between the linear C3D4 and the quadratic C3D10 tetrahedral elements, whereat the usage of the C3D10 element is recommended, because the C3D4 element is too stiff and should only be used if the mesh resolution is sufficient fine. There are four different definitions in ABAQUS for the quadratic C3D10 tetrahedral element: C3D10, C3D10M, C3D10HS and C3D10M (see [9]). Two of these four, the C3D10 and the C3D10I, are relevant for our application. The C3D10M are specially interesting for contact problems and the C3D10HS is used for incompressible materials. The C3D10 is the standard definition of the element with four integration points (see figure 1.4), whereas the integration points for the C3D10HS are at the node locations. This modification is resulting in a better surface stress visualization for the C3D10HS elements.

Chapter 2

Methods

This chapter is giving a short overview of the different available samples and the corresponding test procedures. First the strut samples available will be presented and both the important features of them and the test procedures and tools are highlighted. The following evaluation is giving a short roundup of the most important experiences with the used setup. The methods part for the lattices is giving a short overview of the lattices in the same format as the struts section, a short overview of the available samples with a short description of the test setup followed by a recap of the most important observations.

2.1 Struts

2.1.1 Samples

The strut samples were printed in two groups, of which the first group was printed with geometry-mismatch compensation and the second one without. Group number one contains struts printed in three different orientations: vertical (parallel to printing direction), 45° and horizontal (parallel to the printing plane). The targeted diameter for all the samples of group one is 200 µm, in which the term targeted was used because the samples have nominal diameters smaller than 200 µm. Group two includes struts with the following printing orientations: vertical, 60°, 30° and horizontal. They have four different nominal diameters: 200 µm, 300 µm, 400 µm and 500 µm. All strut samples are printed with support struts which are used to maintain the strut from critical loads, as for example bending, before testing. These support struts are cut directly before starting the test after the clamping of the samples in the test setup. As mentioned in section 1.2.5 is the geometry-mismatch compensation used to reduce the defects depending on the printing orientation. As explained in section 1.2.2 is the printing process melting powder layer by layer to build up the final part. Although the layer

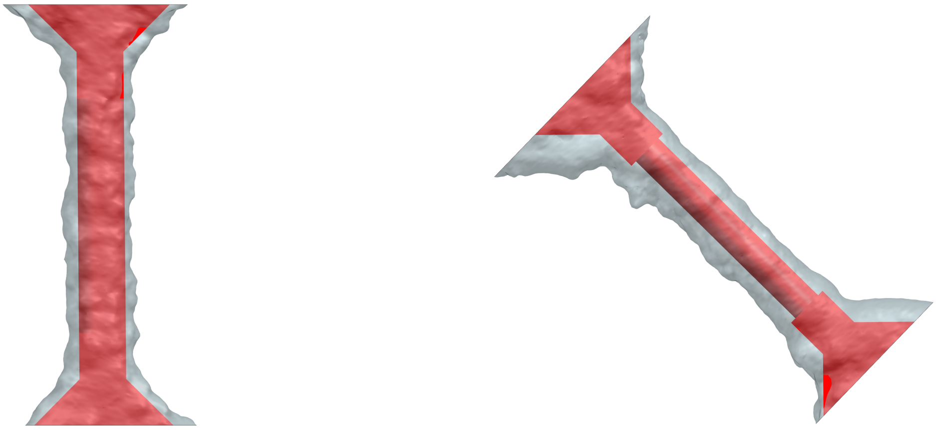

(a) Vertical specimen

(b) 45° specimen

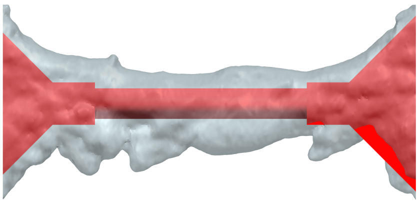

(c) Horizontal specimen

Figure 2.1: Difference between the CAD (nominal) geometry (red) and the printed geometry (grey) for the struts of sample group one.

size is given with 30 µm melts the laser also the underlying layers, which is critical for the first layers of a part because it leads to an increased melted region. The geometry-mismatch compensation, detailed explanation can be found in section 1.2.5, is trying to correct this mismatch by reducing the affected dimensions of the nominal geometry.

2.1.2 Testing Conditions

For the mechanical characterization of the strut specimens a planar biaxial test-machine (MTS Systems Corporation, Eden Prairie, USA) was used. The machine is mounted horizontally and consists of four hydraulic actuators and a possible configuration with load cells up to 2.5 kN. The four axis are aligned as follows: axis one and three, which were used for the sample testing, are perpendicular to axis two and four. For the struts testing a custom built setup was used, consisting of two aluminum clamps and a mounting device, which is used to keep one end of the clamped sample static for the

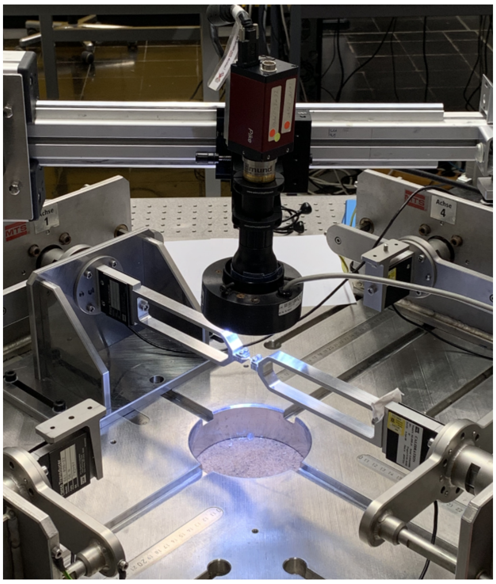

(a) Overview of test setup for the strut testing.

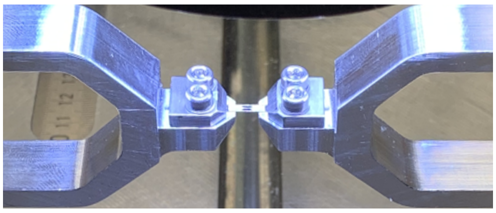

(b) Close up of clamping geometry for strut samples. The different length scales can be nicely seen.

Figure 2.2: Overview and close up of strut sample test setup.

testing. For the force measurement two load cells with a maximum force of 100 N were used. Axis three was used to apply the displacement and the mounting device was installed at the location of axis one. The force was measured with the load cell of axis three, which was mounted at the static end to minimize inertial effects during the measurements.

The tensile tests were conducted cross-head controlled, with a strain rate of $0.000\,25\,\mathrm{s}^{-1}$ for the test specimens. Due to the elasticity of the test setup it was necessary to run test measurements to determine the exact behavior of the used aluminum clamping devices, which strongly affect the final sample strain rate. These measurements were then used to determine the necessary displacement of the cross-head to result in the aimed strain rate, which was $0.007\,\mathrm{mm\,s}^{-1}$. This comparably large displacement rate is necessary due to the long aluminum clamps which are showing a large but linear deformation during the tensile tests.

2.1.3 Digital Image Correlation Setup for the Struts

The strain measurement was conducted with digital image correlation (DIC) due to the size of the test samples, which prevented an efficient implementation of a touching extensometer. The installed DIC setup was consisting of a camera (Pike, Allied Vision, Exton, USA) with a resolution of 1000 x 1000 pixels and a LED ring-panel. Additionally to the existing light source two additional LED spots were used to increase the illumination uniformity of the sample's circular geometry. The software GOM Correlate 2018 was used for amnalysis of the taken images and the strain measurements. The free version of GOM Correlate 2018 was used, which is limited to two dimensional measurements. For the strain measurements GOM allows for placing a virtual extensometer on the sample, which is a critical step for a good strain measurement (see section 2.1.4).

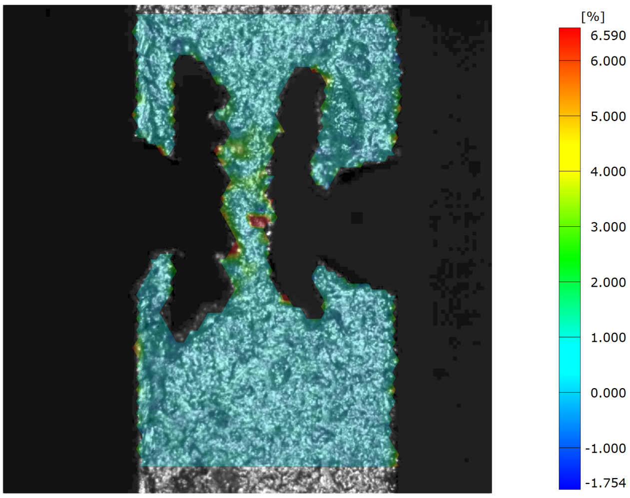

Figure 2.3: Strain distribution of a loaded horizontal strut sample.

2.1.4 Evaluation

The obtained results for the strain measurements highly depend on the correct placement of the virtual extensometer. Typically a tensile test sample has an almost constant cross-section along the gauge length. Due to the previously mentioned characteristics of the additive manufacturing process our samples show a large variation for the cross-section (detailed results in 3.1.2). Upon loading this leads to local plastification and can end up in a decreased elastic modulus. Due to the increasing coefficient of variance for the

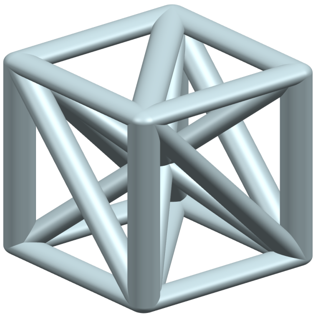

Figure 2.4: Unit cell with applied geometry-mismatch compensation. The adapted diameter for the different orientations can be nicely seen.

thickness towards the horizontal samples a wrong placement of the extensometer can more significantly influence the achieved results. This issue can also be observed looking at the scatter levels in results of the tensile tests for the differently oriented samples. The best results for the strain measurement can be achieved by measuring the strain along the full strut length. Another problem with this measurement is the bending of the test samples, because most of the samples are slightly bended due to the manufacturing process, which is not considered in our measurements and might affect them.

2.2 Lattices

2.2.1 Samples

The lattice samples were printed in one order and two different orientations, namely horizontal and vertical. For both printing directions two different samples were printed. One sample for tensile and compression testing and one for simple shear experiments. All of these samples were printed using the geometry-mismatch compensation.

2.2.2 Unit cell

The unit cell used is a tetrahedron, a stretch dominated lattice structure (see section 1.2.4), with a nominal strut thickness of 200 µm. The unit cell size is 1.2 mm x 1.2 mm x 1.2 mm and it has a nominal porosity of 75 %. This configuration was chosen because [10] showed a good result for the bone ingrowth and biocompatibility for this porosity.

In figure 2.4 we can see the unit cell for the lattices with applied geometry-mismatch compensation. The 45° struts have a decreased cross-section resulting in a elliptical shape with 75 µm and 100 µm radiuses. The horizontal stuts have the following radiuses: 50 µm and 100 µm.

2.2.3 Testing Conditions

For the mechanical characterization of the lattice specimens a uniaxial test-machine was used (walter + bai Testing Machines, Löhningen, CH). The strain measurement was conducted with a 15 mm extensometer (Epsilon Technology Corp, Jackson, USA). For the measurement one load cell with a maximum force of 100 kN was used.

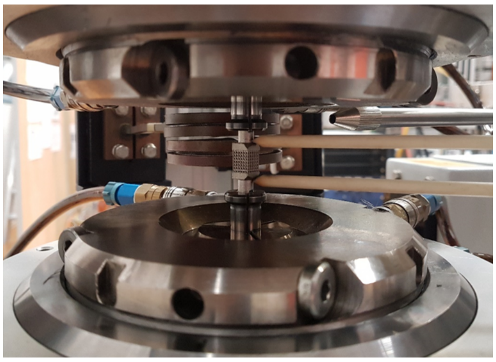

(a) View of a lattice sample with extensometer applied.

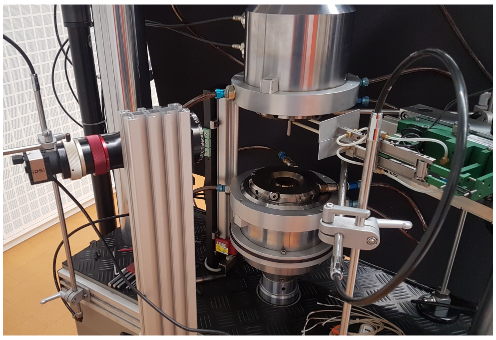

(b) Overview of the lattice sample test setup with extensometer and camera.

Figure 2.5: Lattice sample test setup.

Most of the tests were conducted cross-head controlled with a targeted strain rate of 0.000 25 s^{-1}. This includes the tensile, compression and shear tests. One exception was the incremental loading test, which was force controlled at the beginning with a force rate of 0.1 kN s^{-1}. The extensometer was used for all the tensile tests and additionally for the first samples of the compression and shear experiments, which were used for the digital image correlation (DIC) calibration. The subsequent samples were clamped as long as possible for which reason the extensometer could not be used anymore.

2.2.4 Digital Image Correlation Setup for the Lattices

For additional measurements we also used a DIC setup consisting of a camera (IDS Imaging Development Systems GmbH, Obersulm, Germany) with a resolution of 1280 x 1024 pixels and a 1/1.8″ sensor size. We used a telecentric lens (Edmund Optics Inc., Barrington, USA) with a 0.25X magnification. With this specifications we have a field of view of 28.7 mm and a final resolution of 0.0224 mm per pixel. The first measurements were runned in combination with the extensometer to verify the results of the DIC. The results of one of these comparisons can be seen in figure 2.7. For our experiments no additional speckle pattern was applied, instead the pattern resulting from the coarse surface roughness was used. To avoid significant changes of the speckle pattern due to the change of the light source's incident angle a large homogeneous light source was used. The samples then were illuminated indirectly via the opposite wall. Another difficulty was the precise tracking of the struts and to avoid the false tracking of the struts behind the surface struts.

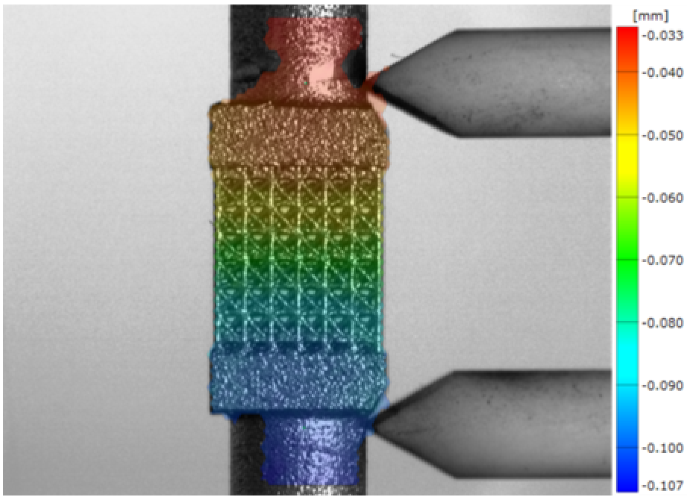

Figure 2.6: Calibration of the DIC with the measured displacement of the extensometer used as reference.

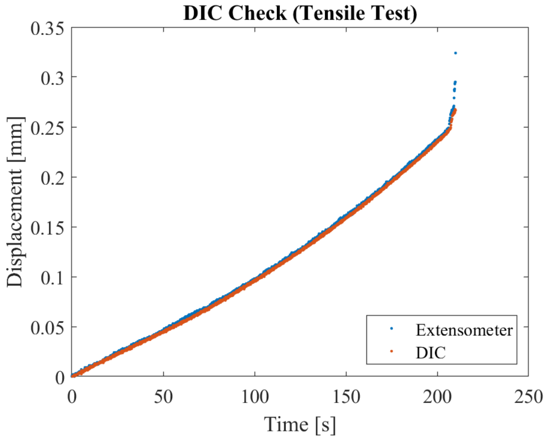

Figure 2.7: Difference of measured displacement of extensometer and DIC.

2.2.5 Evaluation

The results from load cell and extensometer are a good reference for the evaluation of the DIC results. Although we only verify the global results at the location of the extensometer it allows us to check the plausibility of the DIC, which is important for the validation of local strain measurements. One problem for the DIC results was the appearing scatter, local large strains were detected in a frame and not detected anymore in several frames later. Although the values were changing significantly but the location of them was not moving. One possible explanation could be the reflection of the shiny surface of the struts which is highly depending on the illumination angle of the light. Additionally the circular struts are not illuminated over the full surface, which is not possible due to the used light setup, and the scatter is often appearing at the boundaries of the tracking surface. This indicates that the insufficient illumination of the struts is causing the scatter.

Chapter 3

Experimental Results

3.1 Struts

For every sample group six specimens were tested. It was planned to conduct all the test during one session to avoid sensitivity differences in the test setup. The vertical samples start with sample ten. Sample eleven was exposed to large bending during the cutting of the support struts and was therefore replaced by sample sixteen. For the 45° samples (number one to six) all the samples were tested without any failure during the sample preparation. For the horizontal specimens the cutting was critical. Five samples failed during cutting with the pliers. For the additional samples the cutting of the support struts was changed and a Dremel was used instead of a pliers.

3.1.1 Experimental results

Figure 2.1a shows the results for the tensile testing of the vertical struts. All six samples have a maximum force of approximately 60 N and an elongation between 2.5 % and 7 %. The mean value for the force at 1 % strain is 58.43 N with a standard-deviation of 2.04 N and an average maximum elongation of 4.71 % with a standard-deviation of 1.71 %. For the 45° struts we can see a reduced maximum force between 40 N and 60 N and a maximum elongation ranging from 2 % to 4 %. The average maximum force and elongation of the 45° samples are (48.20 ± 4.59) N and (2.89 ± 0.79) %. The maximum force for the horizontal specimens ranges from 35 N to 55 N with a maximum elongation of 3 %. The maximum force for the horizontal samples is (43.01 ± 6.85) N with an elongation of (1.89 ± 0.75) %. Comparing the different results we can see an decreasing maximum force and elongation towards the horizontally printed samples with at the same time increasing scatter. These results can be explained with the observations in section 3.1.2.

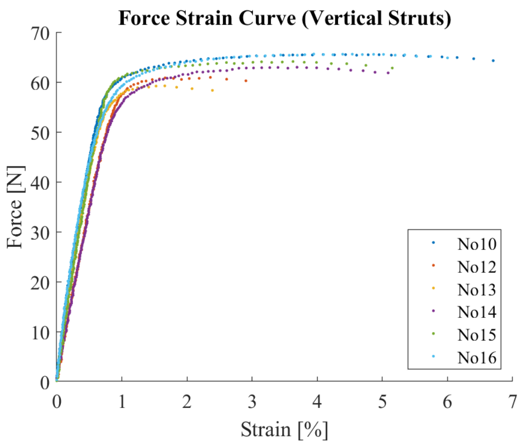

(a) Resulting forces of the tensile test for the vertical specimens. The force values show minimal scatter compared to the other samples. The scatter is significantly worse for the maximum strain.

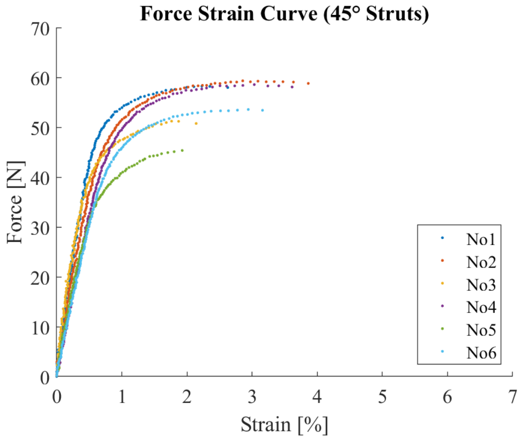

(b) Resulting forces of the tensile test for the 45° specimens. We can see a decreased maximum force with increased scatter compared to the vertical results. The maximum elongation is decreased too.

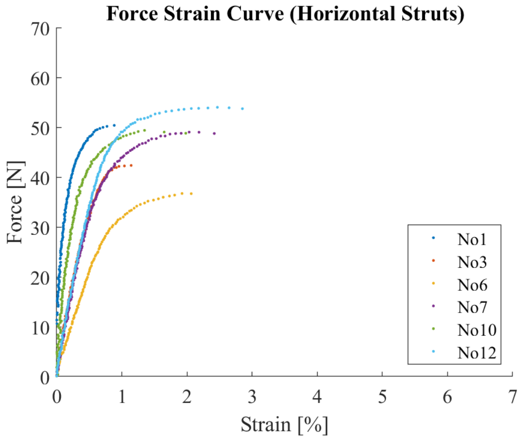

(c) Resulting forces of the tensile test for the horizontal specimens. The maximum force and elongation are decreased further. Noticeable is the large scatter.

Figure 3.1: Tensile testing results for all the samples with different printing directions of group one.

3.1.2 Geometry Analysis

Taking the nominal diameter of the samples for determining the stress strain response resulted in a material behavior which was significantly stronger than expected. The calculated values were almost 50 % higher than the values found in appendix B. The reason for the increased material stiffness and strength can be found in the oversizing of the samples. For every sample to be tested a microscopic picture was taken before testing, which indicated that our samples have a significant oversizing (see figure 3.2). Although the mismatch-compensation was used the oversizing was significant for all the different printing orientations.

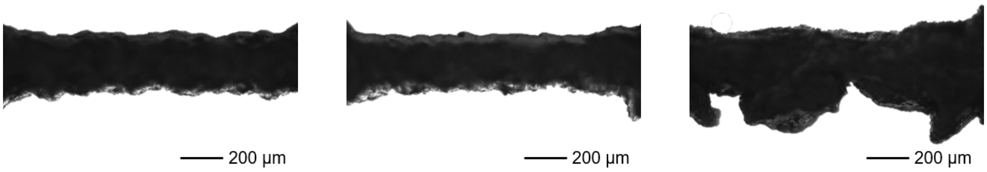

(a) Vertical specimen (b) 45° specimen (c) Horizontal specimen

Figure 3.2: Microscopic pictures of the compensated strut samples. They are a good example for the oversizing of the struts and the variation of cross-section along the strut.

Additionally to the significant oversizing, the struts also have a visible variation of the cross-section. The diameter was varying among the different samples but also along the individual struts. This variation is increasing towards the horizontal samples. Nevertheless, a correct cross-section measurement is crucial for the correct determination of the stress strain curve. For this reason, instead of using the nominal diameters, the microscopic pictures were used to measure the cross-section assuming our samples have a circular cross section. Crucial for the cross-section measurement, especially for the horizontal struts, is the location of the diameter measurement. Obviously the value changes significantly along the sample in figure 3.2c. Two approaches were chosen: using the average diameter or the minimum diameter. For the determination of the average diameter, six measurements equally distributed over the length were taken and the average value was then calculated. The observed differences are discussed in section 3.1.3. The resulting curves for the minimum diameter measurement can be found in figure 3.3.

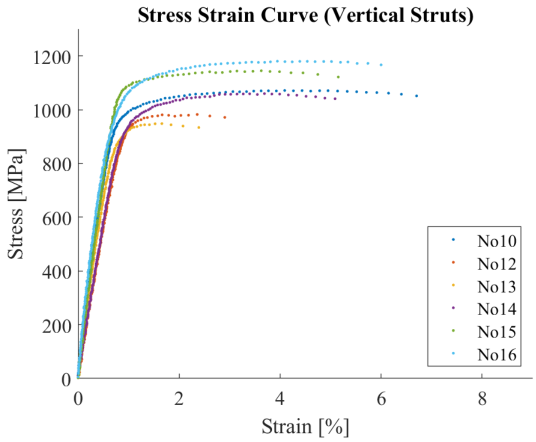

(a) Resulting stress strain curves for the minimum diameter measurement method. The scatter is increased compared to the force strain curves.

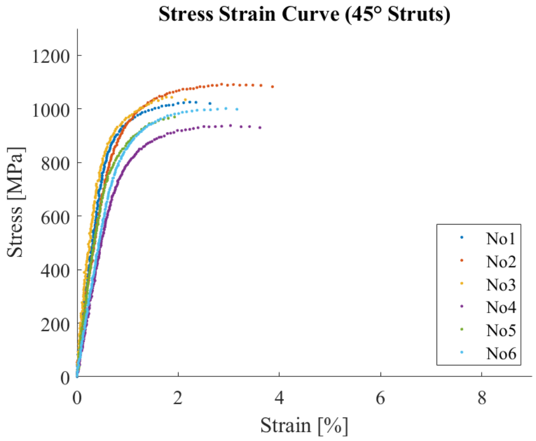

(b) Resulting stress strain curves for the minimum diameter measurement method. The scatter is decreased compared to the force strain curves.

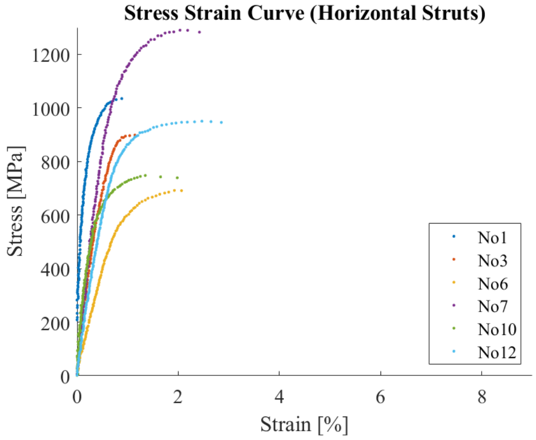

(c) Resulting stress strain curves for the minimum diameter measurement method. The scatter is consistent to the force strain curves. Most of the samples are significantly weaker than expected.

Figure 3.3: Stress strain response of different types of struts. Minimum diameter was considered for determination of cross-section and stress calculation.

3.1.3 Stress-Strain Curves

Whereas the obtained stress strain curves from the two cross-section determination approaches show a small difference for the vertical and 45° samples, a significant change for the horizontal struts was found. The question was which of the two measurement methods is giving us more reliable results. An argument for the method with using the average of several measurements would be that the result is more trustworthy with more than one measurement. But more important would be to consider the expected behavior of the probe during a tensile test. A generalized assumption would be to expect failure at the location of the smallest cross-section. For this reason the preferred measurement method would be to take one measurement at the location of the minimum diameter; especially if we take into account the stated observation at the beginning that the results for the wavy horizontal struts significantly change. We can see that the minimum diameter measurement method improves the results for our horizontal sample. Still the results show a large difference to our expected values and the question arises how precise our measurement methods are actually working.

3.1.4 CT Data Analysis

As it can be seen in section 3.1.3 both of the measurement methods are working quite well for the vertical and 45° samples, but not for the horizontal samples. For the average diameter considerations a significant difference to the expected values, given in appendix B, was observed. A possible answer for this mismatch might be that the sample fails at the location of the smallest cross-section. By consideration of the average diameter, we will have a huge overestimation for our effective cross-section. This is not the case for the method based on the minimum diameter consideration, where we intentionally select the critical location. However we also have a large variance for the different curves derived with consideration of the minimum diameter. This indicates that our measurement method is not working as expected or more precisely that our assumption of a circular cross-section might be wrong.

To be able to precisely determine the material properties a reliable cross-section measurement is crucial. Previous studies showed that the small scale of these samples combined with the limited surface quality can cause a large error for cross-section measurements (see [14]). The approach, presented in this paper, was to determine the material properties by testing strut samples and use these material parameters for lattice structures. They measured the cross-section of their strut samples by using a caliber. The obtained dimension was then called feret diameter. To assure that they can determine the cross-section as precise as possible a relation between feret diameter and actual cross-section was derived. The relation was derived by cutting several samples at different locations and measuring the feret diameter, in this situation the maximum diameter was found, and the actual cross-section. The found correlation worked well for their purpose, but it is important to mention that only vertically printed samples were used in their study.

With the CT data analysis a comparable thought to the mentioned study was followed. The basic idea was to look for a possible correlation of our measured diameter to the actual cross-section. For this purpose the CT data of the different available samples was used. In total eighteen samples of the compensated struts (batch one) and 64 samples of the uncompensated struts were CT analyzed. The eighteen samples of batch one were all scanned together with six samples of every orientation (90°, 45° and 0°). This is mentioned to show that the relation between the different samples was not influenced by the correct grey-value for the CT images. Which might be, although the grey-value was chosen with care, a possible effect for the samples of batch two. A voxel size of 0.005 582 05 mm was used for all three coordinates for the μ-CT of batch one. The samples of batch two were scanned in four groups: 90° (vertical), 60°, 30° and 0° (horizontal). For each sample group, four samples of every diameter were scanned: four times 200 µm, four times 300 µm, four times 400 µm and four times 500 µm. The 90° (vertical) samples were scanned with a voxel size of 0.005 58 mm, the 60° with a voxel size of 0.005 58 mm, the 30° with a voxel size of 0.005 57 mm and the 0° (horizontal) samples with a voxel size of 0.005 66 mm. The 3D geometries were constructed by using Mimics and 3-matic (see section 4.1). The geometry analysis and accurate measurements of the diameter were conducted using the CAD software NX 11 (Siemens PLM, Plano, USA), which can import the generated STL files of the struts.

The first study focused again on the oversizing estimation, which was done previously using the light microscope pictures. For the purpose of the oversizing determination, the CT samples were measured at least for six locations along the strut length (see figure 3.4). The cross section was then measured using NX and an equivalent circular cross-section with diameter d_e was calculated. This equivalent diameter was then compared to the nominal (CAD geometry without geometry-mismatch compensation) diameter d_n to get a oversizing relation r_o (see eq. 3.1), where oversizing is equal to $r_o > 1$ and undersizing is equal to $r_o < 1$. This definition was chosen to have a comparable ratio to the previously conducted studies, regarding the oversizing, using the microscopic pictures.

$$r_o = \frac{d_e}{d_n} \tag{3.1}$$

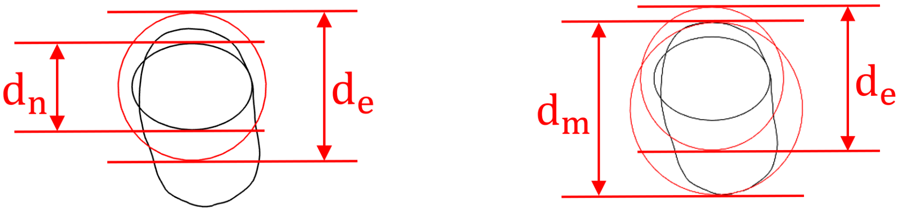

(a) Example of a cross-section and the corresponding equivalent cross-section. The relation of the equivalent diameter d_e over the nominal diameter d_n is representing the oversizing.

(b) Example of a cross-section and the corresponding equivalent cross-section. The relation of the measured diameter d_m and the equivalent diameter is representing the measurement error.

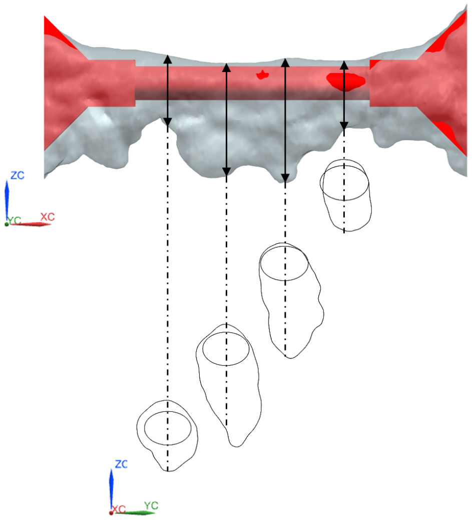

(c) Image of a horizontal sample (grey) with the corresponding nominal geometry (red) representing the view on a sample using the light microscope. The number of measurements is for a better visualization reduced to four.

Figure 3.4: Oversizing measurement of a horizontal sample

The second analysis was conducted to estimate the measurement error, if the microscopic pictures are used to determine the cross-section. For this purpose the CT samples were measured the same way as the microscope pictures. A 2D view was generated identical to the view of the microscope and measured identically. The measured diameter d_m was then compared to the equivalent diameter d_e which resulted in a relation r_m (see eq. 3.2), where $r_m > 1$ indicates an overestimation and $r_m < 1$ an underestimation of the cross-section. The results for the analysis can be seen in figure 3.5 and tables 3.1 and 3.2.

$$r_o = \frac{d_m}{d_e} \tag{3.2}$$

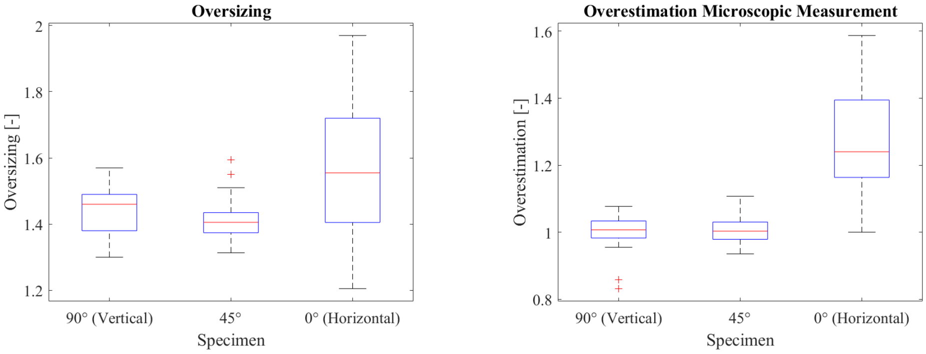

(a) Distribution of the resulting oversizing. Six measurements for six samples per printing direction were taken.

(b) Distribution of the resulting overestimation. Six measurements for six samples per printing direction were taken.

Figure 3.5: Results of the oversizing and overestimation investigation for strut group one. The increased scatter for the horizontal samples can be clearly seen. The overestimation nicely shows why we have a underestimation of the resulting stress-strain curves for the horizontal samples.

	Vertical	45°	Horizontal
200 µm	1.44 ± 0.07	1.41 ± 0.06	1.56 ± 0.20

(a) Oversizing strut group one

	Vertical	45°	Horizontal
200 µm	1.00 ± 0.04	1.01 ± 0.04	1.27 ± 0.14

(b) Overestimation strut group one

Table 3.1: Results of the oversizing and overestimation analysis of the CT data for strut group one.

	Vertical	60°	30°	Horizontal
200 µm	1.41 ± 0.02	1.45 ± 0.04	1.62 ± 0.06	1.65 ± 0.20
300 µm	1.31 ± 0.02	1.36 ± 0.03	1.51 ± 0.08	1.35 ± 0.09
400 µm	1.18 ± 0.01	1.23 ± 0.01	1.31 ± 0.05	1.19 ± 0.08
500 µm	1.14 ± 0.01	1.16 ± 0.02	1.16 ± 0.03	1.14 ± 0.05

(a) Oversizing strut group two

	Vertical	60°	30°	Horizontal
200 µm	1.01 ± 0.03	1.04 ± 0.04	1.21 ± 0.06	1.35 ± 0.12
300 µm	1.01 ± 0.02	1.04 ± 0.03	1.25 ± 0.09	1.27 ± 0.09
400 µm	1.00 ± 0.02	1.06 ± 0.03	1.22 ± 0.06	1.13 ± 0.07
500 µm	1.02 ± 0.02	1.06 ± 0.02	1.14 ± 0.04	1.15 ± 0.09

(b) Overestimation strut group two

Table 3.2: Results of the oversizing and overestimation analysis of the CT data for strut group two.

3.1.5 Scanning Electron Microscope (SEM) Analysis

For a detailed sample analysis, especially of the fracture surface, SEM studies were conducted. The results of these studies are particularly interesting for the fatigue testing. Nevertheless were also tensile samples analyzed to check if we see an unexpected features at the fracture surface. In addition to that, these pictures of the fracture surfaces could be used as reference picture for the fatigue specimens analysis. This was mainly the purpose for the lattice sample analysis. For the strut analysis we tried to find a difference in the fracture surface for different strain values. Unfortunately no distinct difference for the fracture surfaces could be found for the vertical strut samples. But what could be observed was that there is a significant amount of pores at the fracture surface, because almost every analyzed sample had a pore type defect at the fracture surface. This indicates that if we have unexpected results in our optimization it might be due to the presence of pores in the samples. In figure 4.9 we can see an example of the fracture surface of a vertical and horizontal sample.

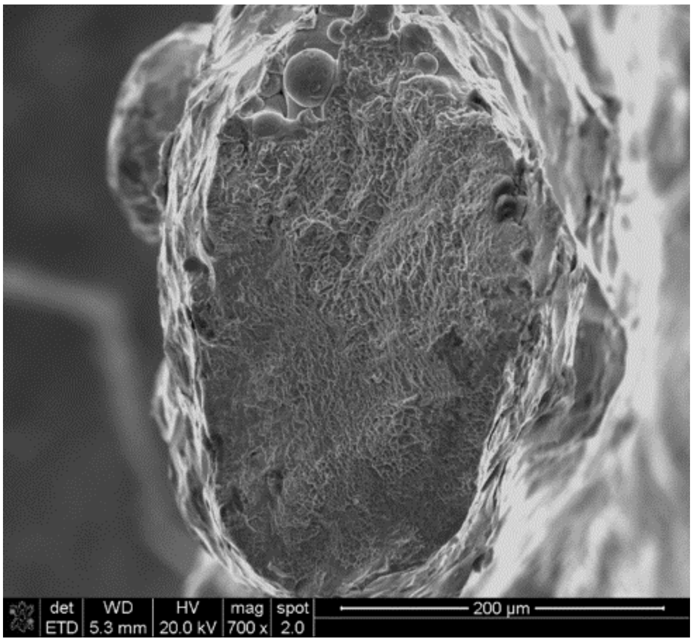

(a) Picture of a horizontal strut sample, where no porous defects can be seen. The elliptical shape can be clearly visible.

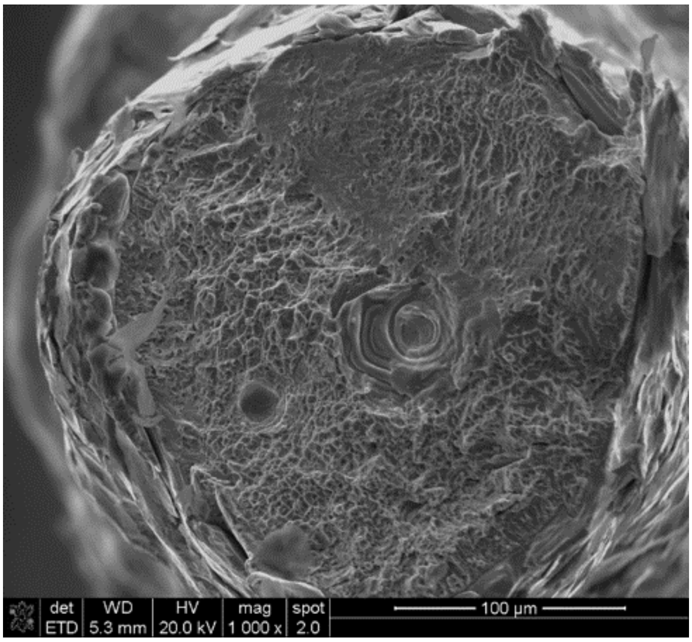

(b) Picture of a vertical strut sample, where the porous defects are clearly visible.

Figure 3.6: SEM pictures of the strut samples.

3.2 Lattices

For the tensile behavior twelve lattices were tested, for each printing orientation (90° (vertical) and 0° (horizontal)) six samples. The displacement of the lattices was measured with the extensometer for all the samples. One vertical sample was used for the incremental testing, where the displacement was measured with the extensometer and DIC. Two vertical samples, one of the CT samples, were used for the compression testing. The first one was conducted with the extensometer attached to the sample. To improve the alignment stability the second sample was then clamped as long as possible (see section 2.1.2) and as a result, it was not possible to use the extensometer. The same procedure was used for the vertical shear samples. Whereas the horizontal shear samples were all tested with long clamping.

3.2.1 Experimental Results - Tension

The tensile testing for the lattices was straightforward for all the samples. The difference between the response of the samples built with the two orientations is decreased comparing to that for the struts (see section 3.1.1). Still the vertical samples are the stronger ones and do show a larger displacement at failure. The maximum force is 7.9 kN with a standarddeviation of 0.33 kN and a maximum displacement of 0.23 mm with a standarddeviation of 0.04 mm. For the horizontal samples the maximum force is (6.30 ± 0.81) kN and the maximum displacement is (0.16 ± 0.02) mm.

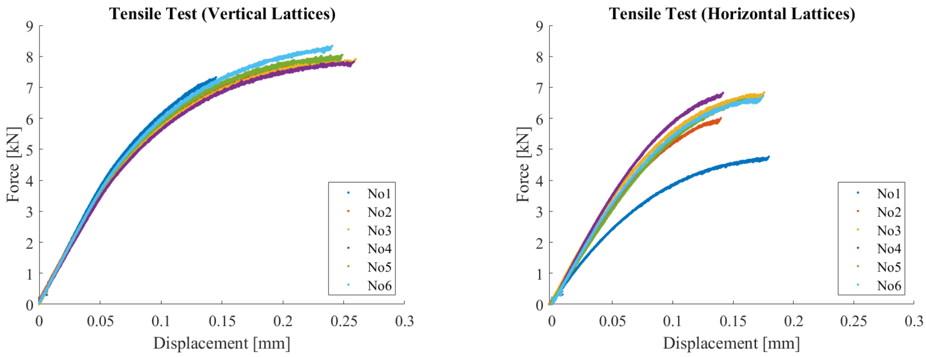

(a) Resulting forces of the tensile tests for the vertical specimens. The values show minimal scatter in force and elongation compared to the horizontal sample.

(b) Resulting forces of the tensile tests for the horizontal specimens. We see decreased force and elongation for the horizontal samples compared to the vertical samples. Additionally we see increased scatter for the force.

Figure 3.7: Results of the tensile tests of the lattice structures for tensile testing displayed as force displacement curves.

3.2.2 Experimental Results - Incremental Tension

The results of the tensile tests show a linear region up to approximately 4 kN. To check if the linear region is actually corresponding to the elastic region an incrementally loaded tensile test was conducted with a vertical sample. The test was conducted, where the sample was initially loaded and unloaded force controlled. The applied load was increased with every cycle by 1 kN up to 5 kN. The upper limit was set based on results of the tensile test. The curves show clearly a non-linear behavior at 5 kN, which indicates a non-negligible plastification behavior at this load level (see figure 3.7a). Additionally this limit was selected be low enough to avoid a force controlled tensile test, which would be unstable at failure of the sample. The results can be seen in figure 3.8.

According to the observations from displacement record of the incremental loading, there is plastic deformation after 3 kN. So although the overall force displacement behavior looks linear up to 4 kN there is already plastic deformation. The plastic hardening of the sample is also nicely visible in figure 3.8. The maximum load of the sample is smaller than expected compared to the previous tests. This might be caused by the sample-to-sample variability or the incremental loading is damaging the sample and therefore the tensile strength decreased.

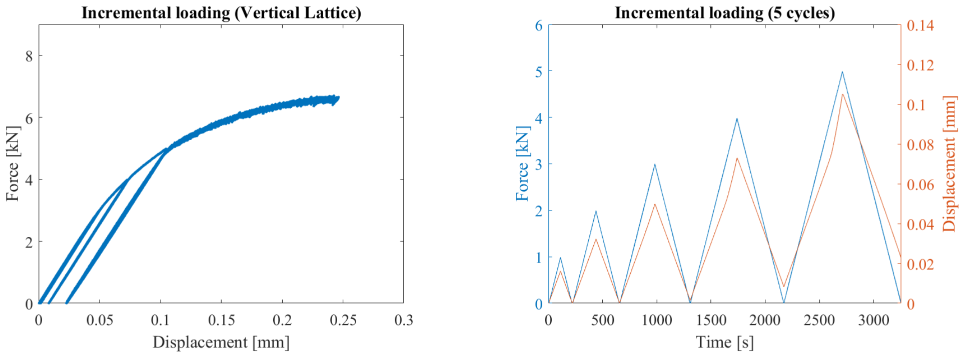

(a) Resulting force displacement curve of the incremental test.

(b) The resulting displacement with the associated force plotted of time.

Figure 3.8: Results of the incremental tensile test of the lattice structure displayed as force displacement curve and displacement with associated force over time. In both plots the plastic deformation can be nicely seen.

3.2.3 Experimental Results - Compression

Compression test for these lattice structures show a very characteristic behavior. During the compression test failing of individual unit cell planes and strain localization can be observed. The goal was to track these planes with the DIC. Two samples were tested, where the first one was tested with the extensometer. For this experiment, some bending was observed. Due to this observation the additional compression test was conducted with a longer clamped length. Figure 3.9 shows the full length of the two tested samples, whereas the right plot is comparing the tension and compression behavior of the two tested CT samples.

The maximum force for the CT sample at failure (reducing force) of the first unit cell group is $-7.8\,\mathrm{kN}$ at a maximum displacement of $-0.27\,\mathrm{mm}$. Comparing the compression results with the tensile results (see figure 3.9b) we can see a comparable behavior.

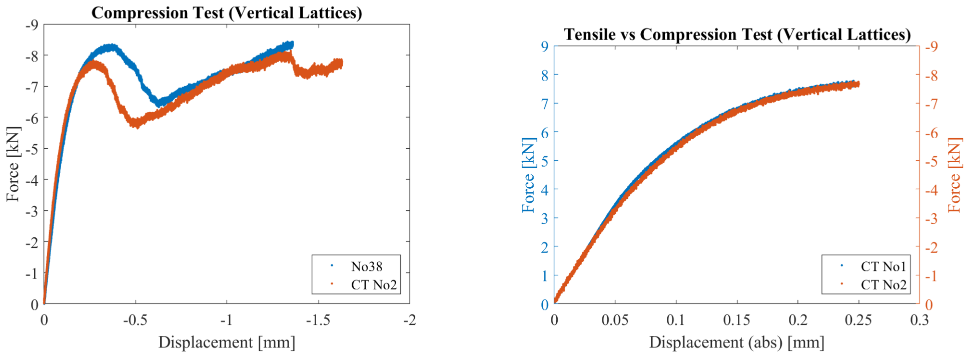

(a) Resulting forces for the compression test. The plot is showing the full length of both conducted compression tests. The step wise failure of the structure can be nicely seen for both tests.

(b) Resulting forces of the tensile test compared to the forces of the compression test. An almost identical behavior for tension and compression was observed.

Figure 3.9: Results of the compression tests of the lattices structures for tensile and compression testing displayed as force displacement curves

3.2.4 Experimental Results - Shear

The experimental shear tests provided further information to verify our material model (see section 4.2.1). The first vertically printed shear sample was tested with the extensometer applied. The sample showed large deformation of the L-shaped attachment geometries, which subjected the sample additionally to bending. To minimize the bending effect the samples were clamped also as long as possible, for which reason the extensometer was removed for the additional tests. The results for the vertically built samples can be seen in figure 3.10a and for the horizontally built samples in figure 3.10b.

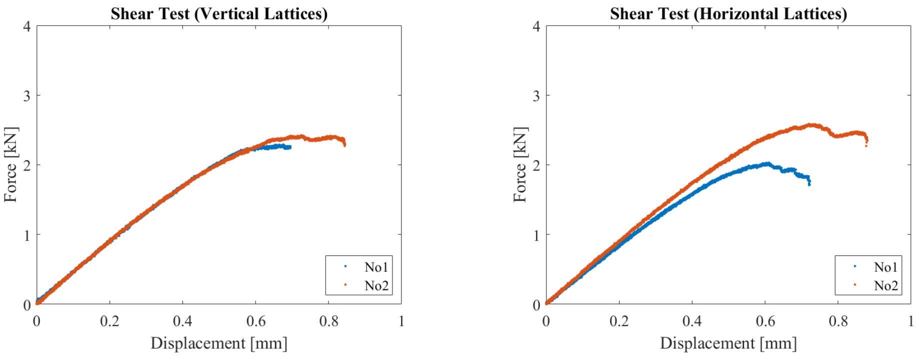

(a) Resulting forces for the shear tests of the vertical shear samples. Both samples fail at a comparable load level with different elongation.

(b) Resulting forces for the shear tests of the horizontal shear samples. The samples fail at a comparable load level as the vertical one but with an increased scatter.

Figure 3.10: Results of the shear tests of the lattice structures for shear testing displayed as force displacement curves.

The force and elongation at failure for the vertical samples are (2.35 ± 0.09) kN and (0.77 ± 0.10) mm and (2.3 ± 0.4) kN and (0.79 ± 0.11) mm for the horizontal samples. During the test, failure at the boundary between solid and lattice section was observed for one of the samples. For further tests it has to be considered that the samples might fail at these locations and some additional samples have to be prepared for this purpose.

3.2.5 CT Data Analysis

In total four CT samples were available, of which two were used for a tension and a compression test, respectively. For all the samples a 3D geometry was generated to also have a possibility to compare the different samples to each other. The samples were mainly compared for the porosity and the resulting mechanical response of the simulations (see 4.3.3). The expected porosity according to equation 1.3 for the nominal lattice structure is 75 % (see [10]). A calculation, using approximated values of the single struts, to verify the porosity results in 76 %, which agrees with the expected porosity of the nominal geometry. For this calculation the material enclosed by the unit cell was calculated approximately. The material consists of four times one fourth vertical struts (edges of the four side walls), eight times one fourth horizontal (edges at top and bottom) struts plus two times one half horizontal struts (diagonal elements top and bottom). Additionally four times one half 45° struts (diagonal elements of the four side walls) and four times 45° struts (diagonal elements through the unit cell). If we take into account the oversizing for the different printing orientations, mentioned in section 3.1.4, we would expect a porosity of approximately 50 %. To measure the actual porosity of the CT samples were used. The results can be seen in table 3.3.

	CT1	CT2	CT3	CT4
Porosity [%]	68	66	62	67

Table 3.3: Measured porosity of the four CT samples. The values are well above the expected porosity, which is calculated based on the oversizing of the strut samples.

As it can be seen our porosity is larger than the estimated one. This indicates that the resulting geometries for the strut and lattice samples do differ. Looking at the outer layers of the lattice samples we can see that the horizontal strut's diameters are significantly reduced and sometimes even not fully printed. Assuming that the struts parallel to the loading direction are mainly carrying the load, this would be a possible explanation for the increased scatter for the horizontal samples.

Chapter 4

Simulation Results

This chapter will provide an overview of the different relevant working steps, simulation setups and results. First the necessary tools to generate 3D data out of the available CT data will be presented and the necessary and important steps are shortly explained. The second part will explain the setup used for the optimization and the purpose of the optimization process itself. The third part will then show how the results of the optimization are further used. Additionally to that some important observations are discussed.

4.1 CT Data

For the 3D model generation from CT data the software package containing Mimics Research 21 (Materialise, Leuven, Belgium) and 3-matic Research 13 (Materialise, Leuven, Belgium) were used. This section will focus on Mimics and how the 3D data is generated, whereas 3-matic will be discussed in section 4.1.1. Mimics is used to generate 3D models using the raw pictures obtained by the CT. For this purpose all the pictures and their information are imported. For the import of the picture data the voxel size has to be defined. The voxel size is the resolution per pixel and the distance between two scanning planes. The picture information consists of the gray-values, which are used to differentiate between different phases. For our case the two phases are the titanium and the surrounding medium, which makes the differentiation easy. All the gray-values of every picture are collected and used to set the threshold to differentiate between the two phases. Because the gray-values might change between the different samples, the threshold is critical to chose. For all the samples the gray-values had a consistent distribution with varying values. For this reason the initial value was chosen by the characteristic distribution. The value was checked by measuring different strut diameter of the samples, which should be in the range of the measured diameter of the microscope pictures from the struts. The gener-

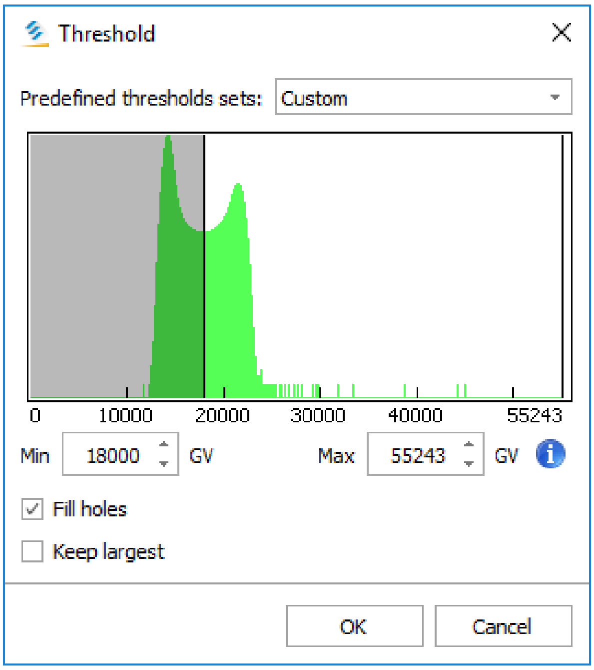

Threshold

Predefined thresholds sets: Custom

Min 18000 GV

Max 55243 GV

☑ Fill holes

☐ Keep largest

Figure 4.1: Gray-value distribution observed for all the strut samples. The lattice structure samples showed an identical behavior. Fill holes was always on because we exported a surface model.

ated selection, containing pixels with a gray-value within the selected range, is called mask. The mask is now containing all the pixels of the set range in every picture, also pixels which might be created due to artifacts or single residual powder grains. To avoid having these geometries in our file we additionally modify the mask with the morphology options. The mask will be reduced by a specified number of pixels, for example if we erode it for one pixel every cross-section will be reduced by one pixel at the outermost layer. If there are single pixels they are removed by this operation. Afterwards the mask will be dilated again for one pixel, which will compensate the previous step on the larger cross-sections. The 3D geometry can now be constructed from the modified mask.

The different voxel sizes for the strut samples was already mentioned in section 3.1.4. For the four lattice samples the following voxel sizes were used. For the first CT sample the voxel size was 0.006 25 mm, for the second sample 0.006 03 mm, for the third sample 0.006 03 mm and for the fourth one 0.006 03 mm. For all the samples the voxel size was identical in all three directions.

4.1.1 Mesh Generation

The 3D geometry generated by Mimics could be exported as STL file, the most common file format in 3D printing environment. It generates a 3D surface model, by triangulation of the corresponding geometry. The first idea was to use ABAQUS for the mesh generation, which would offer the best flexibility regarding mesh adaptions. Unfortunately due to the properties of the STL format an already triangulated surface mesh is imported to ABAQUS. The body generation is possible but then the surface meshing will be affected by the already existing surface triangulation and therefore a very large number of elements was created. Another possibility with ABAQUS is to create a new surface of the existing imported surface mesh. This is not possible due to the complex surface geometry. Additionally to the previous mentioned issues for the lattice structures also the filesize was a problem. Most tried softwares were not able to open STL files larger than 1 GByte. For this reason the 3-matic software from Materialise was used. It is used for meshing and preparing 3D geometries for later 3D printing. It offers the possibility to export a generated mesh to the most common FEA-solver. For our purpose an input-file was generated, which can be imported as part in ABAQUS (only possible since ABAQUS 2018). This mesh is then used to set up the simulation in ABAQUS CAE. Unfortunately this procedure does not allow any changes to the imported mesh, except for the element modification. This could be easily done by modifying the input-file.

Mimics offers the possibility to directly export the generated 3D geometry to 3-matic. The geometry is exported as a surface model to 3-matic. If additional modifications are done in 3-matic, as for example cutting of a geometry the resulting object will have a hole. For this reason too many modifications in 3-matic should be avoided and the appropriate modifications should be done with Mimics. The first step that should be done for the geometry in 3-matic is wrapping. This step reduces the details of the 3D surface model down to a preset value. In our case 0.025 mm, which is the smallest mesh size generated. 3-matic was also used to modify the CT geometry by adding geometrical parts as the boundary blocks. These additional geometries are imported as STL files, which were generated with NX. The different geometries have to be united to a non-manifold assembly, which must be wrapped before it can be meshed. Without wrapping of the created assembly the meshing would not work.

3-matic offers a comparable mesh generation as it is used in ABAQUS CAE. First a surface mesh is generated, where the minimum and maximum element size is specified. Additionally a maximum geometrical error is set, which is determing the maximum deviation of the existing 3D geometry.

The mesh generation uses several iterations, which improve the result but also increase the calculation time. Five iterations is a good compromise and results in already acceptable results. To improve the surface mesh quality the gradient remeshing has to be used. This improves the resulting mesh significantly and is not too time consuming. To generate the volume mesh first the surface mesh has to be checked with the fix interface. The volume meshing will not work as long as there are more than one shell and intersecting triangles. The volume meshing uses the maximum element size and the maximum growth factor as input. The generated mesh can then be exported to a ABAQUS input-file.

An important step in ABAQUS CAE is to check the imported mesh with the mesh check. There might be the possibility that some of the elements are too small and ABAQUS will not run the simulations prompting that some volume elements might have a volume equal to zero. The most efficient solution for this problem is to delete the marked elements. This might lead to singularities but will not affect the overall behavior of the lattice. Another solution would be to change the scale in Mimics, instead of using mm, we could use µm. This step was not used because of the limited time at the end of the master thesis, but is recommended for further analyses.

4.2 Struts

4.2.1 Setup and Optimization

Due to the large mismatches observed for the struts, the precise stress strain curve determination with the in section 3.1.3 mentioned methods is not reliable. For this reason the motivation for this simulation was to calculate the stress strain curve by considering the actual geometry of the tested sample. For this purpose a simulation was set up representing our tensile tests. The geometries needed were meshed with 3-matic using a uniform surface mesh with an edge length of 0.05 mm and a volume mesh with a maximum edge length of 0.1 mm. The elements used are C3D10 (quadratic tetrahedron) elements. The implemented samples consisted of around 10 000 elements. The boundary conditions applied are displacements. For the bottom of the sample all displacements are set equal to zero. This assumption was made because the cross-section is large compared to the strut cross-section and the distance from the strut itself is sufficient. At the top of the part the displacement, corresponding to the maximum measured strain, was applied. The displacement boundary was used instead of force boundary to improve the convergence behavior of the simulation.

Two different material models were used: an isotropic one and an anisotropic

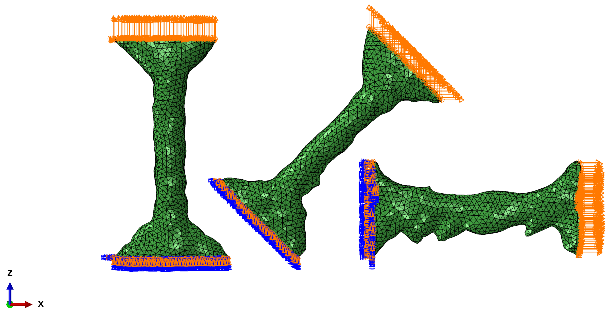

Figure 4.2: Setup for the optimization of the first strut group. The boundary conditions are displacement type.

one. The isotropic material model was used to check for the anisotropic behavior of the material. Five samples were used for this optimization: vertical, 60°, 30° and horizontal of batch two and the 45° sample of batch one. For this purpose for every strut, a different isotropic material model was used for the optimization. For the plasticity behavior, the definition with parameter was used. The results of the optimization showed the need for an anisotropic material model. After this step the anisotropic material model was implemented to the simulation with the corresponding sample group. For the 200 µm struts two optimizations were set up. One with a vertical, a 45° and a horizontal sample of batch one and one with a vertical, a 60°, a 30° and a horizontal sample of batch two. Additionally to these a optimization with the nominal geometries of batch one was prepared to have a correlation factor for the difference between the nominal and the equivalent geometries. Due to the time consuming simulation the optimizations are still ongoing. First results can be seen in figure 4.5.

The results of the simulation was then read out with a python script. To be consistent with the experimental strain measurement two nodes were chosen corresponding to the measurement points of the extensometer used in the software GOM Correlate. The displacement of these points then was used to calculate the strain. For the forces the nodeset, which was used to apply the displacement, was used to calculate the reaction force. These values were then written to a report whose data was further processed using Matlab.

The optimization itself was a fminsearch based function written in Matlab. The fminsearch optimization tries to find a local minimum with a derivative-free method. The script is generating the material input data

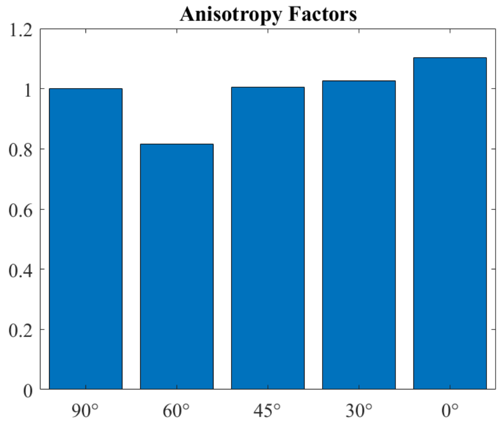

Figure 4.3: Result of the first optimization with all the directions available for 200 µm. The results indicate a difference in the optimized material properties of around 10 %. Based on these results the development of an anisotropic material model was followed.

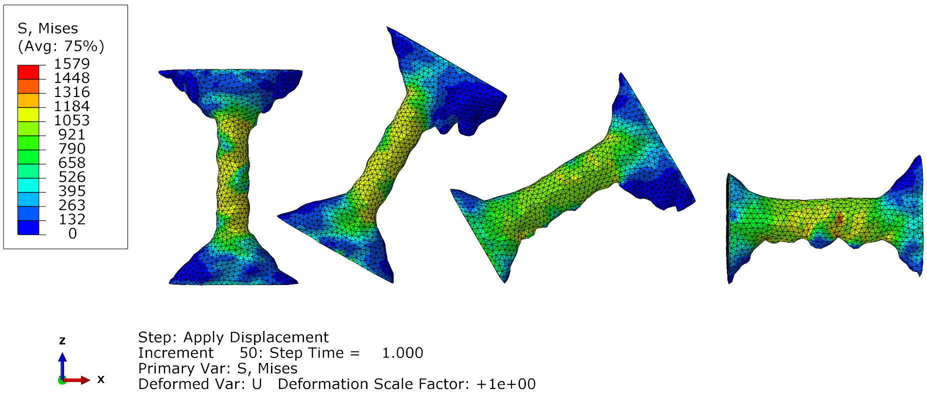

Figure 4.4: ABAQUS model used in the optimization setup for the strut group two. In total 50 incremental steps were used for the analysis.

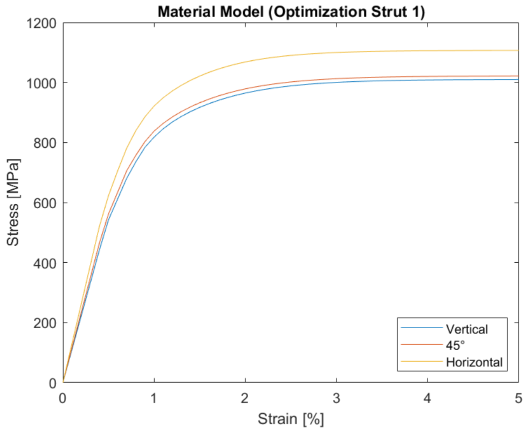

Figure 4.5: Representation of the optimized material model for strut group one. The material model for vertical, 45° and horizontal are shown.

for the ABAQUS simulation. For the linear elastic region three parameters are modified with the script. For the plastic region four parameters for the anisotropic yielding and five for the hardening behavior are used. The Matlab script is using the experimental data and compares it with the results of the simulation. For this purpose the force values of the simulation are interpolated with respect to the strain of the experimental data. The error is then calculated as the difference of the force of the experimental data and the simulation. The error is then squared to calculate the absolute difference. The error for every single sample is then summed up. The resulting error value of every sample is then multiplied with a weighting factor and added up to a total error, which is minimized by the fminsearch.

To plot the optimized material model parameters a simple simulation with five elements representing the different printing directions are used. These elements are used to calculate the stress strain curve, by plotting the Mises stress and the principal strain (see figure 4.5).

4.3 Lattices

4.3.1 Setup

The CT reconstructed geometries were meshed with different element sizes. The surface mesh was generated with the adaptive remesh option. This option is generating a mesh with an element size which is specified with a minimum and maximum edge length. Additionally to these parameters a maximum geometrical error is specified, which is defining the maximum distance between generated mesh and original geometry. This geometrical error was set as large as the smallest detail of the wrapping element, mentioned in section 4.1.1. For all the samples this value was 0.025 mm. To stay consistent with the mesh size of the struts, used for the optimization, a comparable mesh size needed to be chosen. For this purpose the minimum edge length used was 0.05 mm, 0.075 mm and 0.1 mm. The upper limit used for the adaptive remesh was two times the minimum edge length. To decrease the number of surface elements the quality preserving reduce triangles operation was used. With the fix wizard the surface mesh was finished and prepared for the volume meshing. For the volume meshing, a growth factor can be set, which determines the element growth away from the surface mesh. The maximum size for the volume element was chosen to be 0.25 mm and 0.5 mm. The differences between the various meshes are discussed in section 4.3.2.

The simulation of lattices was used to verify the optimized material model parameter. The simulation results are compared to the experimental data of lattice testing. For this purpose the generated FE model had a length of 15 mm, the length of the extensometer. The applied boundary conditions were, similar to the struts, displacements. For the bottom of the sample all displacements were set equal to zero. For the top the displacement in x- and y-direction of the plane were set to zero and the displacement was applied in z-direction. With these simulation setup it is possible to extract the displacement and corresponding reaction force directly of the corresponding nodesets at the bottom or top of the samples. The four CT samples are all vertically printed for tension and compression testing. To also simulate the shear behavior, the shear clamps were constructed using the nominal data with slightly adapted dimensions. The dimensions were changed to suit the printed dimensions. The displacements were applied identical to the tensile sample. The reaction forces of the simulation are extracted at the bottom or top node sets, whereas the displacement is taken from the center of the attachment blocks. This is due to the experimental data, which was not measured anymore with the extensometer but with the DIC setup.

4.3.2 Mesh Sensitivity

The mesh size of the lattice structures were refined step wise to check the convergence of the simulation setup. Starting with the 0.1 mm mesh, which is a relatively coarse mesh with approximately 400 000 elements. The 0.075 mm mesh has around 700 000 elements and the 0.05 mm mesh has around 1 500 000 elements. The fine mesh is about the maximum possible number of elements, which can be used for calculations on Euler due to the maximum usable memory of 128 GByte. All these samples have a maximum volume element size of 0.5 mm. If the volume element size is changed, the number of elements changes significantly. For example employment of a volume el-

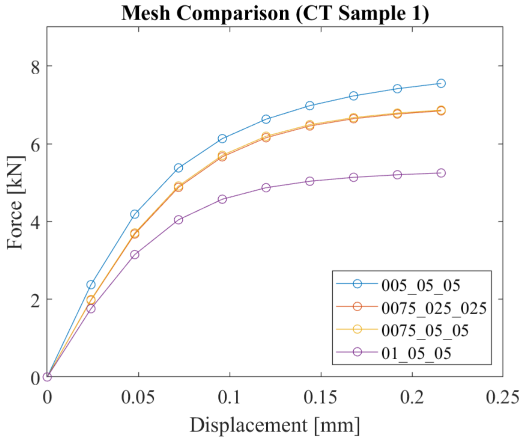

Figure 4.6: Comparison of the reaction force of different meshes. A finer mesh is resulting in an increased reaction force. A change of the volume mesh size has almost no effect on the result.

ement size of 0.25 mm instead of 0.5 mm increase the number of elements by a factor of two. The reason for this are the large clamping regions at the bottom and top of the lattice structures. Figure 4.6 is showing a comparison of different meshes and the resulting forces.

The results of the different simulations show an increasing reaction force with decreasing element size. The expected behavior for a mesh refinement would be a decreasing reaction force. At the same time, we see that a change of the maximum volume element size does not affect the reaction force of the simulation. Due to the applied growth factor, the volume elements will increase with decreasing distance from the surface mesh. So the surface mesh is affecting the size of the first volume elements. This indicates that the volume elements used in the struts of the lattice structure will always be smaller than the maximum volume element size. For this reason the change of the volume mesh size is not affecting the lattice behavior and is resulting in an identical reaction force. Nevertheless, we have an increasing reaction force with decreasing mesh size. This aspect has to be further investigated to have a definite explanation.

4.3.3 Mesh Induced Geometry Mismatches

To check the repeatability of the mesh generation process it was tested for sample one and two if there is a significant change of the lattice behavior. For this purpose the meshes were generated two times from the same CT data with the same parameters from scratch. A minimum variation due to the meshing procedure is expected. The volume variation of the two samples was within 1 %, which is within the expected range. This indicates that the mesh generation is subjected to certain variation, which have to be further investigated, especially for changing mesh size. First observations with struts with different mesh sizes showed higher stress concentrations at coarser meshed samples and an increased reaction force.

4.3.4 Element Type

As discussed in section 4.3.2 we have an increasing reaction force for increasing mesh fineness. A possible first estimation is to check the lattice performance with the same mesh size but different element types. If we change our element type from the used quadratic tetrahedron (C3D10) to the linear tetrahedron (C3D4) we commonly would expect an increased reaction force. In our case, if we assume the mesh depend on the level of discretization, the simulation should actually give us a reduced reaction force. If this is the case the discretization process is inducing the inverted stiffness behavior. If not we can assume that our inverted behavior is induced due to the different volume. First results showed that the linear mesh definition increases the resulting reaction force, which indicates that the dependency is most probably geometry induced. Additionally to the change of the elements to linear ones, another idea was to use an element with a different formulation to check the influence of the element formulation. In section 1.6 the different advantages of the relevant element definitions are shortly discussed. According to this the C3D10I element formulation was considered, which might improve our results. The simulation with the C3D10I element definition showed a small improvement of the FE model behavior but increased the calculation effort significantly. For this reason the C3D10I definition should only be used for the final results.

4.3.5 Comparison Experimental Data and FEA

To judge the performance of the optimized material model, two CT lattice samples were tested to be compared with the outcome of the FE analysis. One with a tensile test, the second one with a compression test. Additionally, a FE model of a shear sample was generated with the available CT data to validate our material model for shear loading. The validation is done by comparing the force displacement curves of the experimental and simulation data. The material model used was from the optimization of strut group one and used the CT reconstructed geometry for the lattice samples. The FE models showed good consistency with the results for the tensile and compression tests, with the largest deviation around the yielding region. The shear sample showed a large difference for the FE model and the experimental data.

The FE model is providing a good representation of the experimental data for tensile tests. The largest difference to the experimental data is found

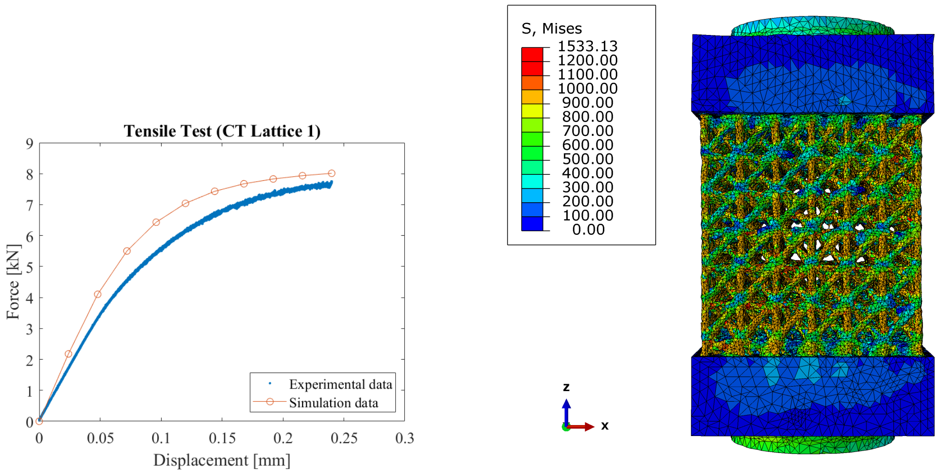

(a) Experimental data compared to the obtained simulation results for latest material model (see figure 4.5). The FE model shows good results for the tensile behavior.

(b) Resulting stress distribution of the lattice under tensile loading. The vertical struts are the struts with the highest stresses.

Figure 4.7: Simulation data for CT sample one under tensile loading.

at the yielding region. This might be improved with the use of additional exponential terms for the plasticity behavior (see section 1.5.2). The FE prediction is within a 10 % margin of the experimental data.

The compression behavior of the FE model is a fairly good representation of the experimental data. At the beginning and at the end, we have the best consistency. Again the behavior around the yielding region is showing the largest differences. The same inconsistency between FE and experimental data for compression and tensile loading indicates that the inconsistency is certainly originated from the model. The FE model does not show the large deformation as the experimental sample does, which might lead to the increased reaction force close to yielding. The experimental sample does show large expansion at around yielding, which might be initiated by the imperfect alignment of the sample in the experimental setup. This is not the case for our lattice sample in the simulation, which is explaining the increased reaction force during compression, due to the improved alignment the FE model is behaving stiffer than the experimental result.

The FE model for the shear simulation is performing the worst. The reaction force is around 150 % higher than the experimental force. Additionally, we observe an exponential behavior for the FE results where the experimental results are still in linear shape. The reason for this behavior is not clear to us yet. Due to the generation of the shear FE model with CT data from the tension and compression samples the most outer layer is not identical to the printed shear samples. Due to this mismatch, a direct comparison might be wrong. Also an direction dependent shear behavior can not be excluded at the moment. The geometry of the lattice unit cell implies that the shear behavior is direction dependent. This could be verified by an additional simulation where the lattice structure is reoriented. Unfortunately the simulation results are not available for this thesis but should be investigated for the ongoing project. Another discrepancy which might affect the results of the FE simulation is the shear modulus obtained by our optimization. We know that we can not determine the shear modulus with our experimental data obtained for the struts. Nevertheless is our optimization also specifying a shear modulus, which might be too high and is effecting our lattice simulation significantly. Additional information regarding the shear behavior can be found with the optimization set up for our lattices. First simulations with a material model with decreased shear modulus are giving us improved results. If we reduce our shear modulus by 50 % we get a consistent result with our experimental data. The goal is now to find a way to improve the result for our obtained shear modulus and verify if there is no direction dependent behavior.

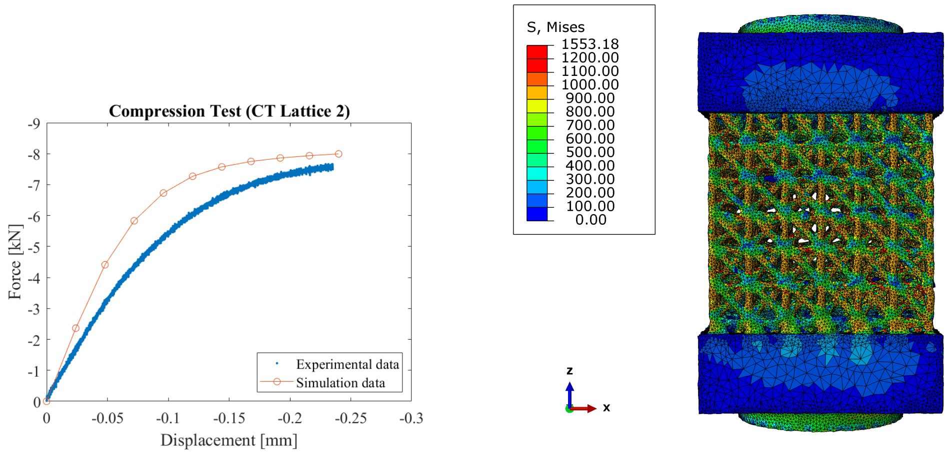

(a) Experimental data compared to the obtained simulation results for latest material model (see figure 4.5). The FE model shows too stiff results around yield for the compression behavior.

(b) Resulting stress distribution of the lattice under compression loading. The vertical struts are the struts with the highest stresses. No significant deformation visible.

Figure 4.8: Simulation data for CT sample two under compression loading.

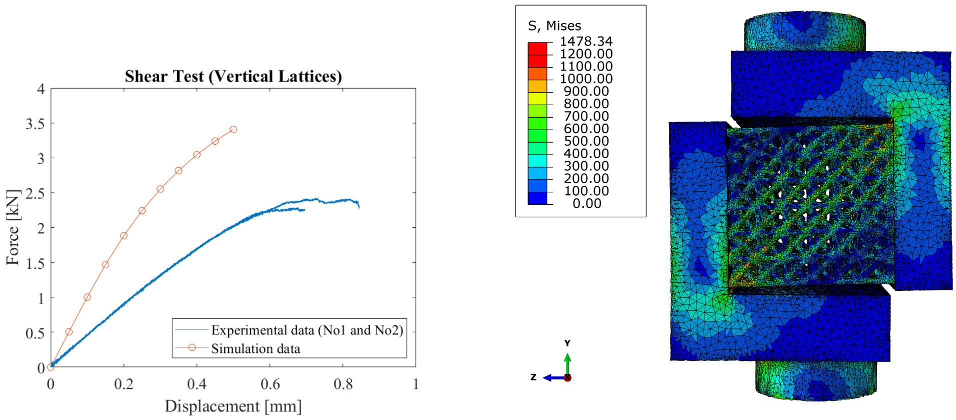

(a) Experimental data compared to the obtained simulation results for latest material model (see figure 4.5). The FE simulation is calculating force values which are too high.

(b) Resulting stress distribution of the lattice. The 45° struts are the ones with the highest stress values.

Figure 4.9: Simulation data for the shear FE model generated with CT sample one.

4.3.6 Comparison DIC and FEA

This section presents a quantitative comparison of the strain calculations of the DIC and the FEA. This offers the possibility to validate the DIC results regarding the strain level and corresponding locations and to estimate possible measurement errors. Additionally it ia a control for both calculations for their plausibility. If both calculations show strains with a comparable size and distribution, one can assume that the two methods are showing plausible results. This is the case for all our measurements (see figure 4.10, 4.11 and 4.12). By comparing the corresponding distributions, we can also locate possible errors for the DIC measurements. The tensile test show comparable results regarding strain size and location except for the struts perpendicular to the loading direction. The DIC measurement is showing large strains for these struts, because many of these values are at the border, it can be assumed that these are errors indicated by the speckle pattern (see section 2.2.5). This behavior can also be observed for the compression test, where we have negative strains at identical locations, which confirm the assumption that these values are errors of the DIC. For the shear test an identical strain localization and size can be found for the two measurements. The quantitative comparison showed that the DIC system shows comparable results to the FEA results, but is affected by errors especially at the boundaries of the tracking region. The strain measurement within the tracking region itself is working well and the measured strains look plausible.

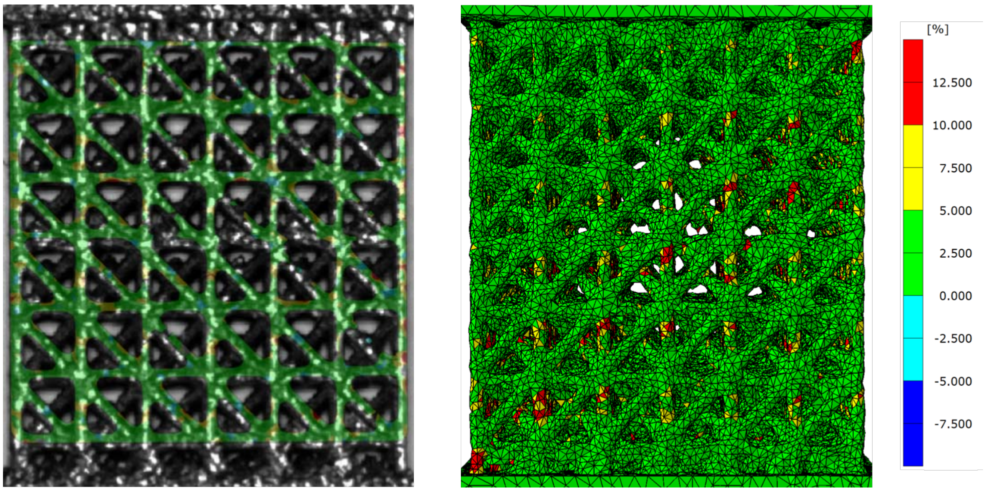

Figure 4.10: Comparison of the strain distribution for the tensile test at 0.24 mm displacement of the DIC (picture left) and the FEA (picture right). Both measurements show a similar strain distribution with the largest strains at the struts parallel to the loading direction. The strain measurements for the struts perpendicular to the loading direction differ, which is caused by measurement errors of the DIC.

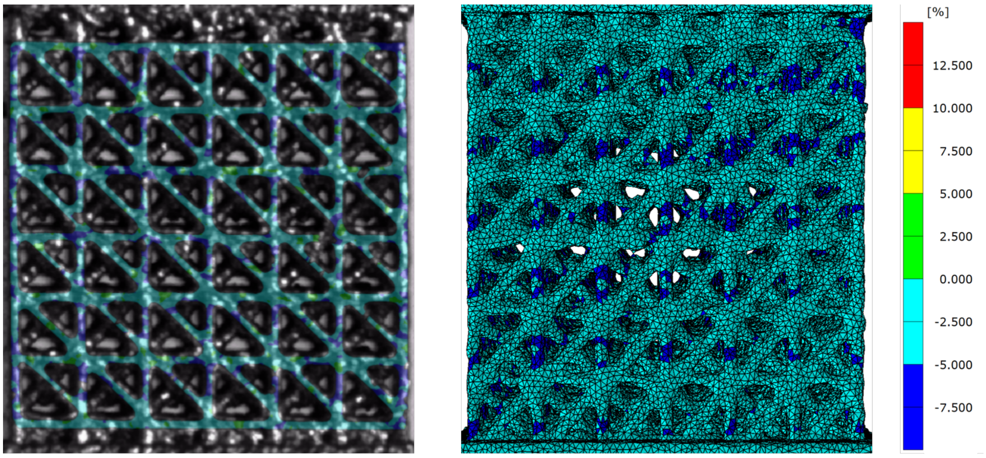

Figure 4.11: Comparison of the strain distribution for the compression test at -0.24 mm displacement of the DIC (picture left) and the FEA (picture right). Both measurements show a similar strain distribution with the largest negative strains at the struts parallel to the loading direction. The strain measurements for the struts perpendicular to the loading direction differ again, which is caused by measurement errors of the DIC.

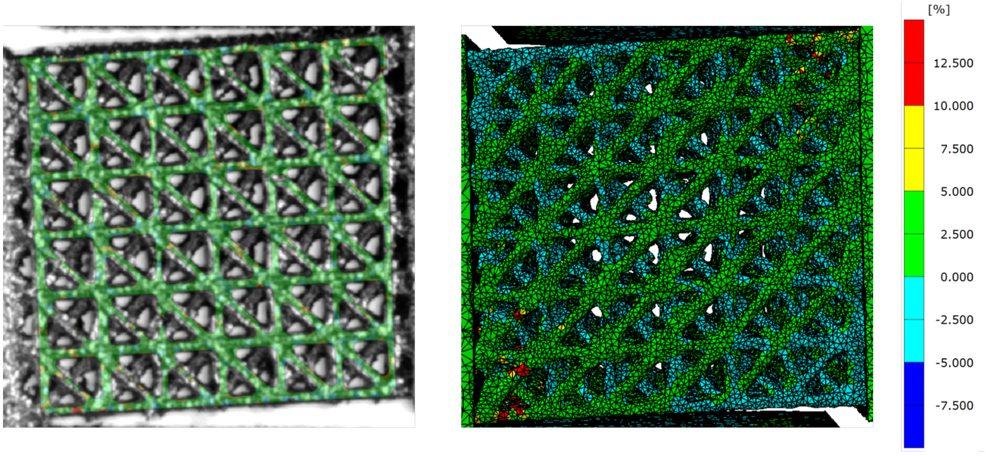

Figure 4.12: Comparison of the strain distribution for the shear test at 0.5 mm displacement of the DIC (picture left) and the FEA (picture right). The orientation of the diagonal struts are different for the DIC and the FE model which might cause different strain distribution and lattice response. Nevertheless are the largest strains located at the same edges for both calculations.

4.3.7 Setup and Optimization

The purpose of this optimization was to extract the material behavior of the unit cells based on the experimental data. Another reason was that there was a clear mismatch for the shear loading between the experimental data and the simulation. The general setup can be seen in figure 4.13. The idea was to replace the unit cells with quadratic brick elements (C4D20). The four different samples were modeled and placed with their respective printing orientation. For the error calculation, force displacement curves were used. Apart from that the optimization was set up identically to the strut optimization. The error resulting from the comparison of the experimental data and the simulation is minimized using the fminsearch function. The interesting point from this optimization is that we get additional information regarding the shear behavior of the lattice structure. Due to this optimization we have the information about the homogenized deformation behavior of the unit cell. This offers us the possibility to analyze the data at a different size-scale.

	E_1/E_2	E_3	G_{13}/G_{23}
Unit cell	15.2 GPa	13.7 GPa	1.5 GPa

Table 4.1: First results of the optimization for the lattice structures with the modulus for the elastic behavior.

The three coefficients for the linear behavior of a unit cell can be found in table 4.1. The values obtained for the homogenized response are approximately eight times weaker than the obtained values for the material model except for the shear modulus, which is almost 30 times weaker than the shear modulus of the material model. This is another indicator that there is a problem with the obtained shear modulus of our optimization. Additionally we have information that can be used for the estimation of additional possible experimental setups.

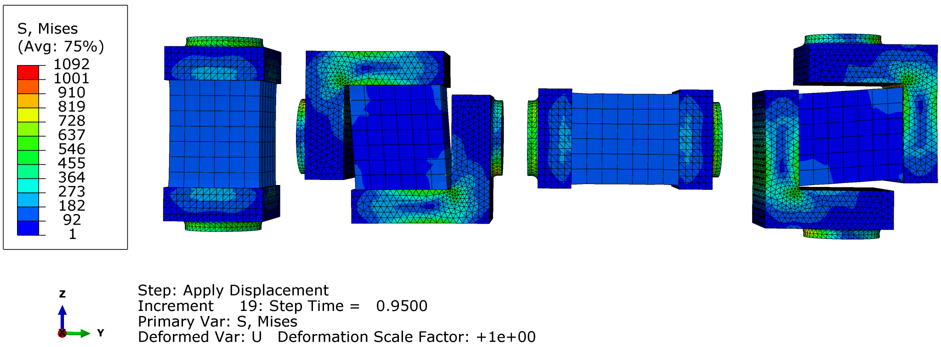

Figure 4.13: Optimization setup for lattices. The samples are arranged as the following: vertically printed tension, vertically printed shear, horizontally printed tension and horizontally printed shear. For the force displacement curves, the experimental data of the vertical and horizontal tensile and shear tests were used (without CT data).

Chapter 5

Conclusion and Outlook

5.1 Experimental Results

5.1.1 Struts

The tensile tests for the strut samples of group one, printed using geometry-mismatch compensation, showed a decreasing maximum force and increasing scatter from the vertically printed towards the horizontally printed samples. During the data analysis, multiple problems, notably the strain measurement and cross-section determination, were found and the relevant conclusions are discussed in this section.

The elongation measurement of the different struts is challenging. Especially to avoid considerable scatter of the measured strain, a consistent method has to be used. Due to the large coefficient of variation of the geometries, local effects have to be considered, especially for the samples with smaller diameters and horizontal printing direction. One important conclusion is to place the extensometer in the GOM software in a way that the fracture location is enclosed. This limits the sample selection to the ones which fail clearly within the gauge length. Samples which fail at one of the ends of a strut should not be considered because the strain measurement might be affected by the transition. Additionally to avoid local effects, the full length of the strut should be considered for the strain measurement.

The determination of the cross-section without using CT data is not very precise. The two dimensional measurement method based on microscopic pictures, assuming a circular cross-section, is giving us acceptable results for the samples with printing orientations vertical, 60° and 45°. For the printing orientations 30° and horizontal, the measurement method is not working sufficiently good. The reason for that was discussed in the CT data analysis section (see 3.1.4), where the two dimensional measurement method based on microscopic pictures was validated by using the available CT data. The analysis showed a good result for the samples printed with an angle larger than 45 %. A preliminary evaluation showed that there is a relation between overestimation of the calculated and measured diameter for the two dimensional analysis, which might be used to improve the microscopic measurement method. The overestimation relation is derived based on the CT data analysis and the microscopic measurement. At the moment, a linear regression is used for the relation and additional data is necessary to further improve the reliability of the relationship.

The stress strain curve determination without the usage of the CT data is difficult and several parameter affect its precision. We have found that it is possible to derive acceptable stress strain curves for samples with a build orientation angle larger than 45°. The result for the stress strain curve determination is mainly affected by the two previously mentioned points, i.e. the strain measurement and the cross-section determination. Another important point is the density of the printed samples. Although the density of the material is expected to be above 99 %, a single pore might affect the tensile strength significantly due to the small scale of the samples. The SEM investigations indicated presence of pore-type defects at the fracture site of many samples, which respectively affect their tensile strength.

5.1.2 Lattices

The tensile testing showed comparable results for the tensile testing as for the struts. Decreased force and displacement to failure, increased scatter were observed for the horizontal samples. To estimate the initial yield point, an incremental tensile test was conducted. Plastic deformation was observed after an applied force of 3 kN although the force displacement curves remains linear up to 4 kN. The under incremental loading tested sample performed worse during the subsequent tensile test, which might indicate that there was already damage formation during the incremental loading.

The compression tests showed that a good and stiff alignment is crucial, because a misalignment affects the initial failure behavior during the compression tests. The compression test showed impressively the step wise failure of the different unit cells. Comparing the force displacement curves of the tension and compression tests showed an identical force displacement behavior for the lattices for tension and compression (see section 3.2.3).

The shear tests showed again the importance of a stiff and precise test setup. The samples showed increased scatter for the force values of the horizontal samples and large scatter in maximum displacement for both sample orientations. The reason for the increased scatter might be due to additional deformation of the clamping region. The similar force at failure indicates that we do have a comparable shear behavior for our unit cells along the horizontal and the vertical direction.

5.1.3 Digital Image Correlation

The DIC used for the struts to measure the strain showed good results but a precise and consistent usage is crucial to minimize the possible measurement error. Due to the circular cross-section of the strut samples the installed light source is illuminating the sample not sufficiently good. With the additional light sources, two small LED spots placed at the side, used, the resulting pattern was improved considerably.

The DIC used for the lattice testing showed good results for the large scale displacement measurements. So the DIC can be used as a reliable replacement for the extensometer. The displacement measurement is also effective for the local scale to track displacement of the different struts of the lattice structure. The strain measurement is working sufficiently good for tracking of local strain localizations with a reasonable strain level. But there is also a scatter visible generated by two major facts: the lighting and the speckle pattern. Due to the usage of the surface roughness of the sample, the generated speckle pattern is quite coarse and affected by the location of the light source. Using a large light source to avoid a significant lighting angle dependency the circular cross sections of struts of the unit cells are not sufficiently covered and the strain measurement is restricted to the illuminated region. An improved speckle pattern with enhanced illumination might give better results for the local strain measurement. An additional limitation is given due to out of plane displacement, which limits the DIC usage to a certain amount of deformation. This limit can be to some extent increased with the previous mentioned improvements, i.e. an improved speckle pattern and improved illumination.

5.2 Simulation

5.2.1 Material Model Optimization

Due to the issues with the conventional methods for determining the stress strain curves, the FE based optimization was set up for derivation of the material model. The simulations involved in the optimization are costly, due to the small elements size which is necessary to avoid geometrical mismatches, especially for the plastic regime. For this reason, the optimizations are still ongoing and only preliminary material models could be derived. An important observation was that the obtained material model parameters change between the different sample sizes and groups (see 4.2.1). This is due to the scatter, which was observed during the tensile testing of the strut samples and is affecting the optimizations. To minimize the influence of scatter in the data an optimization setup with all the samples might be necessary. The optimization for the strut group one is showing consistent results with the material data given by Renishaw (see B).

The so far obtained material models of the different sample groups showed a substantial variation. One of the reason for this is the fact that always only one sample per orientation was used. As we have seen in the experimental results, the experimental results include a significant scatter. To minimize the effect of the scatter of a single tested sample an optimization using all the samples is recommended. The biggest challenge is to choose a representative material model formulation for the printed material.

5.2.2 Material Model Performance

The preliminary material model obtained from the strut group one was used in the FEA for the representation of the deformation behavior of the lattices. The FE model was able to represent the deformation response of the lattices well, particularly for the tensile and compression loading. The slightly decreased model performance for the compression might be due to differences in the alignment considerations, which is resulting in a increased stiffness for the FE model. The model performance for the shear sample is insufficient. The resulting forces for the simulation are over 50 % higher than the measured results. This might be due to a unrepresentative derivation of the shear modulus or unreliability of the material model. For this reason, further investigations regarding the shear behavior of the lattice structures are necessary.

One problem for the lattice samples was the uncommon mesh dependency of the resulting reaction forces. The observation made, was that with increasing fineness of the mesh an increasing reaction force was resulting. Preliminary investigations are indicating that the problem is caused due to geometrical differences of the various mesh sizes. These differences might be resulting from the high complexity of the original CT data, where the resolution of the mesh might be critical.

5.3 Outlook

The major difficulty for the experiments with the struts is the precise measurement of the cross-section. For a reliable determination of the stress strain curve, the cross-section determination is crucial. For this reason it is important to further investigate how the cross-section measurement could be improved. An analytical relationship might be derived to estimate the cross-section from two dimensional microscopic examination. Another important task to fully understand the strut behavior would be a metallurgical investigation, because the material properties are highly affected by the different phases. The phase composition on the other side is highly affected by the temperature history of the parts, which might be crucial for the used samples (see section 1.2.3).

The lattice sample testing showed the different behavior for the two printing orientations. The incremental tensile test and the compression tests were only done with vertical samples. It would be interesting to also have the experimental data for the horizontal samples for incremental and compression loading. To further validate the material model, additional CT data should be generated; at least for two horizontal samples to run a tensile and a compression test. To further validate the shear behavior a vertical and horizontal shear CT scans could be helpful.

The DIC setup for the lattices provides results, which are allowing a first estimation of the overall deformation behavior. The resulting strain distributions were compared with the corresponding FE model and showed consistent values. One critical topic is the scatter in the DIC data which is induced by the current setup. An improved speckle pattern could be developed by applying an artificial pattern to the lattice surface. The difficulty is to have a reliable method to apply such a pattern in such a scale and to verify the results of the DIC.

The optimizations showed varying results for the different sample groups for this reason all the sample groups should be combined in one optimization. Additionally to minimize local effects for the strain measurement a far field displacement measurement should be used for the samples. This means the displacement measurement with GOM should be taken not at the strut but as far away of it as possible, to avoid the local effects (see section 2.1.4). To avoid a local minimum the algorithm fminsearch can be exchanged by another optimization function. To improve the plastic representation additional exponential terms should be used.

The material model performance might be improved with the usage of the lattice sample testing. The obtained deformation behavior of the unit cell shows a significantly low shear modulus. By using unit cells instead of the overall lattice, a setup of an optimization is possible which is optimizing the material model with the additional information of the tension, compression and shear tests of the lattices. Additionally the usage of the unit cell scale FE models could give a better insight to the difficulties faced with the lattice meshing and might explain the mechanism causing the uncommon mesh dependencies.

Bibliography

[1] Alexander E. Wilson-Heid, Shipin Qin and Allison M. Beese. Anisotropic multiaxial plasticity model for laser powder bed fusion additively manufactured Ti-6Al-4V. 2018.

[2] M.J. Cross, G.J. Roger, and J. Spycher. 7 - Cementless fixation techniques and challenges in joint replacement. In *Joint Replacement Technology*, pages 186 – 211. Woodhead Publishing, 2014.

[3] Dassault Systèmes Simulia Corp. SIMULIA User Assistance 2018, 2018.

[4] Edoardo Mazza. Continuum Mechanics 1 - Script, 2017.

[5] Ehsan Hosseini. Metal Additive Manufacturing - Lecture 1 - Introduction to Additive Manufacturing, 2019.

[6] V. S. Deshpande et al. Foam Topology Bending versus Stretching Dominated Architectures. 2000.

[7] J. Y. Cho, W. Xu, M. Brandth and M.Qian. Selective laser melting-fabricated Ti-6Al-4V alloy: Microstructural inhomogeneity, consequent variations in elastic modulus and implications. 2018.

[8] Jingjing Yang, Hanchen Yu, Zemin Wang, Xiaoyan Zeng. Effect of crystallographic orientation on mechanical anisotropy of selective laser melted Ti-6Al-4V alloy. 2017.

[9] Optimec Consultants. Tetrahedral elements available in ABAQUS for structural analysis? When to use what?, available at: http://optimec.ca/news/tetrahedral-elements-available-abaqus-structural-analysis-use/ [12.08.2019].

[10] Sajad Arabnejad, Burnett Johnston et al. High-strength porous biomaterials for bone replacement: A strategy to assess the interplay between cell morphology, mechanical properties, bone ingrowth and manufacturing constraints. 2015.

[11] Shunyu Liu, Yung C. Shin. Additive manufacturing of Ti6Al4V alloy: A review. 2018.

[12] Wenjin Tao and Ming Leu. Design of lattice structure for additive manufacturing. pages 325–332, 08 2016.

[13] X. Wang, J.S. Nyman, X. Dong, H. Leng and M. Reyes. 4 - Mechanical Behavior of Bone. In *Fundamental Biomechanics in Bone Tissue Engineering*. Morgan and Claypool, 2010.

[14] Zhiyong Wang, Peifeng Li. Characterisation and constitutive model of tensile properties of selective laser melted Ti-6Al-4V struts for microlattice structures. 2018.

Appendix A

Project Description

ETH
Eidgenössische Technische Hochschule Zürich
Swiss Federal Institute of Technology Zurich

IWF
Institut für Werkzeugmaschinen und Fertigung
Institute of Machine Tools and Manufacturing

Master Thesis
Deformation analysis and finite element modelling for Ti-6Al-4V additive manufactured lattices

Background

Metal Additive Manufacturing (MAM) opens completely new opportunities for design and manufacture of biomedical implants with improved mechanical biocompatibility and osseointegration. The possibility of manufacturing fully porous and lattice-structured implants allows reducing the stress shielding and bone resorption; a typical problem with solid implants causing implant loosening.

Optimization of designs for such biomedical implants require an accurate and reliable understanding of the mechanical response of the lattice structures (e.g. stiffness and fracture strength)


Burn et al (2016)

Fig.1: Bone resorption due to stress shielding effect.

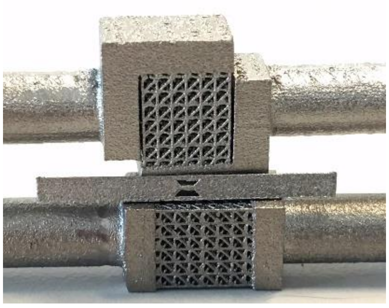

Fig.2: additive manufactured strut and lattice testpieces.

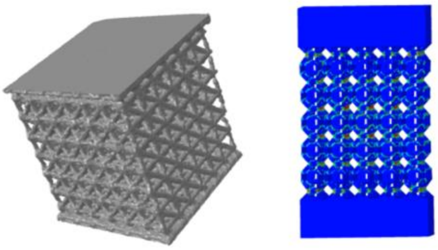

Fig.3: CT reconstructed and finite element model of lattice samples.

Task description

In a first step, the student shall familiarize him/herself with the concepts of computer tomography and digital image correlation, as they will be used for characterization of the as-built geometry of testpieces and strain measurements during mechanical testing. The other components of the project include mechanical experiments, analysis of data, development of constitutive model and finite element modelling.

Tasks

1. Literature research
2. Use of computer tomography data for construction of FE models
3. Mechanical experiments
4. FE analysis

Division of work: 10% Theoretical Background, 15% Experiments / Validation, 65% Data Analysis and FEA 10% Documentation

Kick-off: 01.02.2019

Supervision

Dr. Ehsan Hosseini HTIG/Empa Tel. 058 / 765 26 66 ehsan.hosseini@empa.ch

Empa
Materials Science and Technology

Appendix B

Material Data

Ti6Al4V ELI-0406 powder for additive manufacturing

Process specification

Powder description	Titanium alloy powder
Layer thickness	30 µm and 60 µm
Laser power	200 W
Additive manufacturing system	AM250

Material description

Ti6Al4V ELI-0406 alloy comprises titanium mass fraction up to 90% alloyed with aluminium up to 6.75% and vanadium up to 4.5%, along with other minor elements. Ti6Al4V grade 23 is otherwise referred to as Extra Low Interstitial (ELI) with regards to the interstitial impurities oxygen, carbon, and nitrogen. It is a higher purity version of the most commonly used titanium alloy Ti6Al4V grade 5. The reduced interstitial elements in grade 23 lead to an increase in both ductility and fracture toughness.

Ti6Al4V ELI-0406 has excellent specific strength (strength to weight ratio) which makes it an ideal choice where weight saving load structures are required. It has good corrosion resistance, it is also biocompatible, so can be used for a range of surgical and dental applications. For medical and dental applications Renishaw supplies Ti DG1 powder, for more infomation refer to document H-5983-9026.

Material properties

- High specific strength
- High corrosion resistance
- Excellent biocompatibility
- Good osseointegration
- Low thermal expansion
- Low thermal conductivity

Applications

- Medical and dental (Refer to document H-5983-9026)
- Aerospace and defence
- Motor sport
- Jewellery and art
- Maritime applications
- High-end sports equipment

Generic data - wrought material

Density	4.42 g/cm^3
Thermal conductivity	6 W/mK to 8 W/mK
Melting range	1635 °C to 1665 °C
Coefficient of thermal expansion (see note 1)	8×10^{-6} K^{-1} to 9×10^{-6} K^{-1}

Note 1	In the range of 0 °C to 100 °C.
Note 2	Annealed at 850 °C ±10 °C for 2 hr.
Note 3	Tested at ambient temperature to ASTM E8. Machined before testing. Values based on a sample size of 6.
Note 4	Tested to ASTM E384-11, after polishing.
Note 5	Tested to JIS B 0601-2001 (ISO 97), after bead blasting.
Note 6	HIP (hot isostatic pressing).

Composition of powder

Element	**Mass (%)**
Titanium	Balance
Aluminium	5.50 to 6.50
Vanadium	3.50 to 4.50
Iron	≤ 0.25
Oxygen	≤ 0.13
Carbon	≤ 0.08
Nitrogen	≤ 0.05
Hydrogen	≤ 0.012
Yttrium	≤ 0.005
Residuals	≤ 0.10 each, ≤ 0.40 total

*ASTM standard composition powder. Renishaw powders are supplied to a tighter specification to minimise batch-to-batch variations. Results quoted in this data sheet are from samples produced using Renishaw's tighter specification powder. Please contact Renishaw for further information about specifications or if you require support in qualifying non-Renishaw powders.

Mechanical properties of additively manufactured components processed in 30 µm layers

	Heat treated (See note 2)		**HIP treated** (see note 6)	
	Mean	**Standard deviation ($\pm 1\sigma$)**	**Mean**	**Standard deviation ($\pm 1\sigma$)**
Ultimate tensile strength (UTS) (See note 3)				
Horizontal direction (XY)	1089 MPa	7 MPa	1033 MPa	4 MPa
Vertical direction (Z)	1085 MPa	12 MPa	1034 MPa	7 MPa
Yield strength (see note 3)				
Horizontal direction (XY)	1007 MPa	5 MPa	947 MPa	4 MPa
Vertical direction (Z)	985 MPa	23 MPa	923 MPa	21 MPa
Elongation at break (See note 3)				
Horizontal direction (XY)	16%	1%	16%	1%
Vertical direction (Z)	14%	1%	17%	1%
Modulus of elasticity (see note 3)				
Horizontal direction (XY)	129 GPa	7 GPa	127 GPa	3 GPa
Vertical direction (Z)	126 GPa	15 GPa	125 GPa	4 GPa
Hardness (Vickers) (see note 4)				
Horizontal direction (XY)	368 HV0.5	10 HV0.5	352 HV0.5	9 HV0.5
Vertical direction (Z)	372 HV0.5	7 HV0.5	360 HV0.5	7 HV0.5
Surface roughness (R_a) (See note 5)				
Horizontal direction (XY)	4 µm to 6 µm			
Vertical direction (Z)	4 µm to 7 µm			

Density of additively manufactured Ti6Al4V is typically 99.8%, measured optically on a 10 mm × 10 mm × 10 mm sample at 75× magnification.

Renishaw plc

Stone Business Park
Brooms Road, Stone
Staffordshire, ST15 0SH
United Kingdom

T +44 (0)1785 285000
F +44 (0)1785 285001
E uk@renishaw.com

www.renishaw.com

RENISHAW
apply innovation™

Mechanical properties of additively manufactured components processed in 60 µm layers

	Heat treated (see note 2)		**HIP treated** (see note 6)	
	Mean	**Standard deviation (±1σ)**	**Mean**	**Standard deviation (±1σ)**
Ultimate tensile strength (UTS) (see note 3)				
Horizontal direction (XY)	1091 MPa	6 MPa	1052 MPa	3 MPa
Vertical direction (Z)	1084 MPa	8 MPa	1058 MPa	9 MPa
Yield strength (see note 3)				
Horizontal direction (XY)	1020 MPa	25 MPa	957 MPa	2 MPa
Vertical direction (Z)	987 MPa	22 MPa	973 MPa	24 MPa
Elongation at break (see note 3)				
Horizontal direction (XY)	16%	1%	16%	1%
Vertical direction (Z)	17%	1%	18%	1%
Modulus of elasticity (see note 3)				
Horizontal direction (XY)	132 GPa	9 GPa	127 GPa	3 GPa
Vertical direction (Z)	128 GPa	7 GPa	131 GPa	6 GPa
Hardness (Vickers) (see note 4)				
Horizontal direction (XY)	363 HV0.5	11 HV0.5	361 HV0.5	7 HV0.5
Vertical direction (Z)	363 HV0.5	13 HV0.5	360 HV0.5	10 HV0.5
Surface roughness (R_a) (see note 5)				
Horizontal direction (XY)	3 µm to 4 µm			
Vertical direction (Z)	5 µm to 7 µm			

Density of additively manufactured Ti6Al4V is typically 99.8%, measured optically on a 10 mm × 10 mm × 10 mm sample at 75× magnification.

For worldwide contact details, please visit www.renishaw.com/contact

Issued: 06.2017

Appendix C

Camera Specifications

UI-1240SE-C-HQ (AB.0010.1.46400.24)



■ Made
■ in
■ Germany

Spezifikation

Sensor

Sensortyp	CMOS Color
Shuttersystem	Global-Shutter / Rolling-Shutter / Global-Start-Shutter
Charakteristik	Linear
Sensor-Auslesemethode	Progressive Scan
Auflösungsklasse	SXGA
Auflösung	1,31 MPixel
Auflösung (h x v)	1280 x 1024 Pixel
Seitenverhältnis	5:4
ADC	10 Bit
Farbtiefe (Kamera)	8 Bit
Optische Sensorklasse	1/1,8"
Optische Fläche	6,784 mm x 5,427 mm
Optische Sensordiagonale	8,69 mm (1/1,84")
Pixelgröße	5,3 µm
Hersteller	e2v
Sensorbezeichnung	EV76C560ACT
Verstärkung (Gesamt/RGB)	4x/4x
AOI horizontal	selbe Bildrate
AOI vertikal	erhöht die Bildrate
AOI Bildbreite / Schrittweite	16 / 4
AOI Bildhöhe / Schrittweite	4 / 2
AOI Positionsraster horizontal, vertikal	2 / 2
Binning horizontal	selbe Bildrate
Binning vertikal	selbe Bildrate
Binning Methode	M/C automatisch
Binning Faktor	2
Subsampling horizontal	-
Subsampling vertikal	-
Subsampling Methode	-
Subsampling Faktor	-

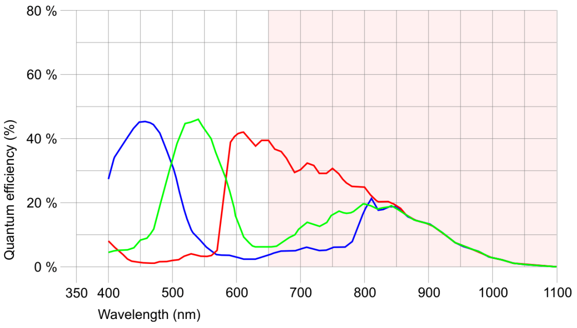

Technische Änderungen vorbehalten (2019-09-08)

UI-1240SE-C-HQ (AB.0010.1.46400.24)

Modell

Pixeltaktbereich	7 MHz - 35 MHz
Bildrate Freerun-Modus	25
Bildrate Trigger (maximal)	24
Belichtungszeit min - max	0.009 ms - 2000 ms
Leistungsaufnahme	0,3 W - 0,7 W
Besonderheiten	Scaler, Sequenzer, Log-Mode, Sensorseitige Hotpixel-Korrektur, Feines Belichtungsraster, Multi-AOI

Umgebungsbedingungen

Die genannten Temperaturen bezeichnen die äußere Gerätetemperatur des Kameragehäuses.

Gerätetemperatur während des Betriebs	0 °C - 55 °C / 32 °F - 131 °F
Gerätetemperatur während der Lagerung	-20 °C - 60 °C / -4 °F - 140 °F
Luftfeuchtigkeit (relativ, nicht kondensierend)	20 % - 80 %

Anschlüsse

Schnittstellen-Anschluss	USB 2.0 Mini-B, verschraubbar
I/O-Anschluss	9-polige Mikro D-Sub-Buchse (MPE Garry 11-0021-50-09L)
Spannungsversorgung	USB-Kabel

Pinbelegung I/O-Anschluss

1	Blitz-Ausgang, mit Optokoppler (-)
2	Trigger-Eingang, mit Optokoppler (+)
3	Schirmung
4	USB-Versorgungsspannung (VCC) 5 V
5	USB-Masse (GND)
6	Blitz-Ausgang, mit Optokoppler (+)
7	Trigger-Eingang, mit Optokoppler (-)
8	USB-Daten (+)
9	USB-Daten (-)

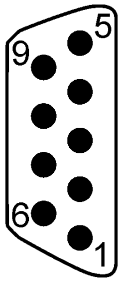

Sicht auf Kamera

Bauform

Objektivanschluss	C-Mount
Schutzart	IP30
Abmessungen H/B/T	34,0 mm x 32,0 mm x 41,3 mm
Gewicht	65 g

Technische Änderungen vorbehalten (2019-09-08)

UI-1240SE-C-HQ (AB.0010.1.46400.24)

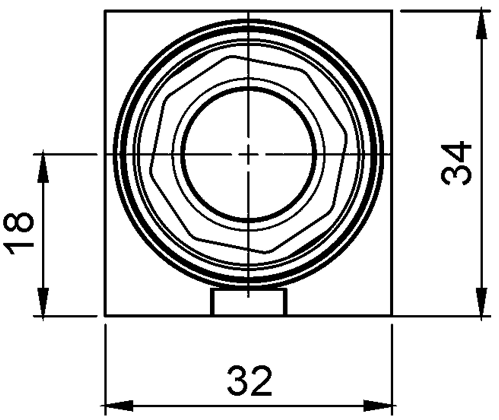

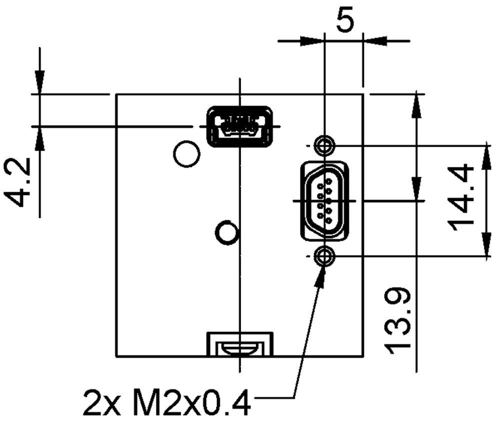

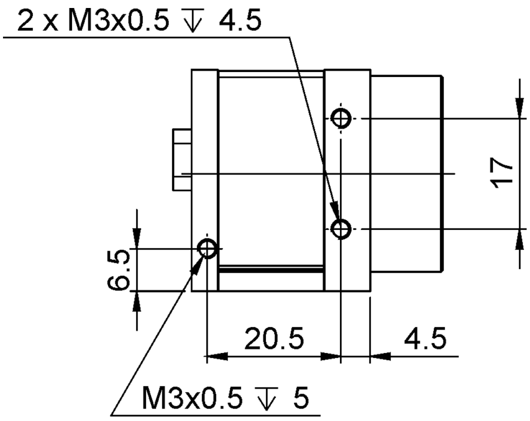

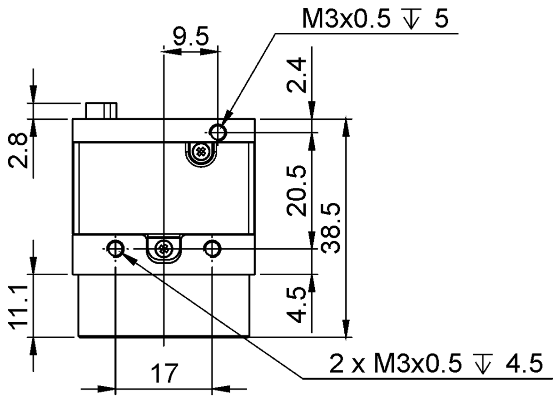

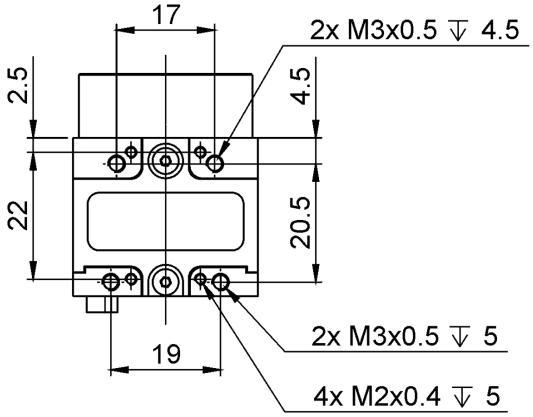

Appendix D

Lens Specifications

TECHSPEC® GOLD SERIES FOCUSABLE TELECENTRIC LENS

#55-349 • 161 - 186mm WD • 0.25X

Important tools for machine vision systems and metrology applications, TECHSPEC® Gold Series Focusable Telecentric Lenses yield images from which precise measurements can be taken. These lenses yield constant magnification over a defined depth of field and are optimized to provide <0.2° telecentricity when used in the specified working distance range. Anywhere within the specified working distance, the same magnification can be obtained simply by refocusing. Both the aperture and focusing adjustment positions can be fixed by set screws to remain secure in high vibration environments.

Primary Magnification:	0.25X
Working Distance[1]:	161 - 186mm
Depth of Field[2]:	±8.2mm at f10 (20% @ 20 lp/mm)
Length:	196.3mm
Filter Thread:	M72 x 0.75
Max. Sensor Format:	⅔″
Camera Mount:	C-Mount

Telecentricity:	<0.1°
Distortion:	<0.5%
Resolution[2]:	>55% @ 40 lp/mm
Aperture (f/#):	f/6 - f/25, lockable
Object Space NA:	0.021
Number of Elements (Groups):	10 (7)
AR Coating:	425 - 675nm BBAR
Weight:	1.44kg

Sensor Size	¼″	⅓″	1/2.5″	½″	1/1.8″	⅔″	1″	4/3″
Field of View[3]	14.4mm	19.2mm	22.8mm	25.6mm	28.7mm	35.2mm	N/A	N/A

1. From front of housing 2. Image space MTF contrast 3. Horizontal FOV on standard 4:3 sensor format

Specifications subject to change

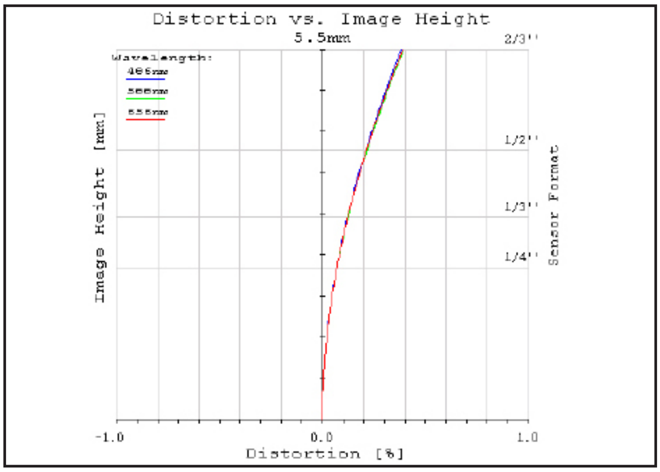

Figure 1: Distortion at the maximum sensor format. Positive values correspond to pincushion distortion, negative values correspond to barrel distortion.

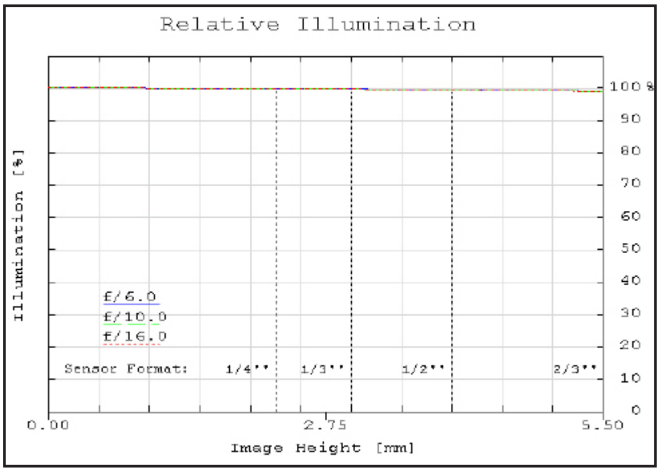

Figure 2: Relative illumination (center to corner)

In both plots, field points corresponding to the image circle of common sensor formats are included. Plots represent theoretical values from lens design software. Actual lens performance varies due to manufacturing tolerances.

TECHSPEC® GOLD SERIES
FOCUSABLE TELECENTRIC LENS

#55-349 • 161 - 186mm WD • 0.25X

MTF & DOF: f/6.0

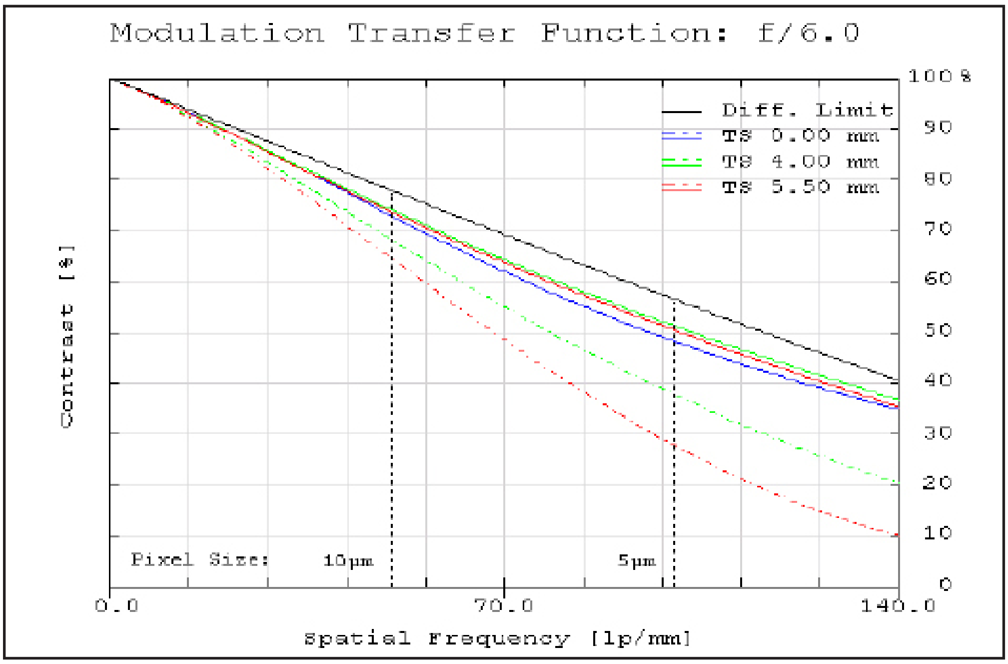

Figure 3: Image space polychromatic diffraction FFT Modulation Transfer Function (MTF) for λ = 486nm to 656nm. Included are Tangential and Sagittal values for field points on center, at 70% of full field and at the maximum sensor format. Solid black line indicates diffraction limit determined by f/#-defined aperture. Frequencies corresponding to the Nyquist resolution limit of pixel sizes are indicated.

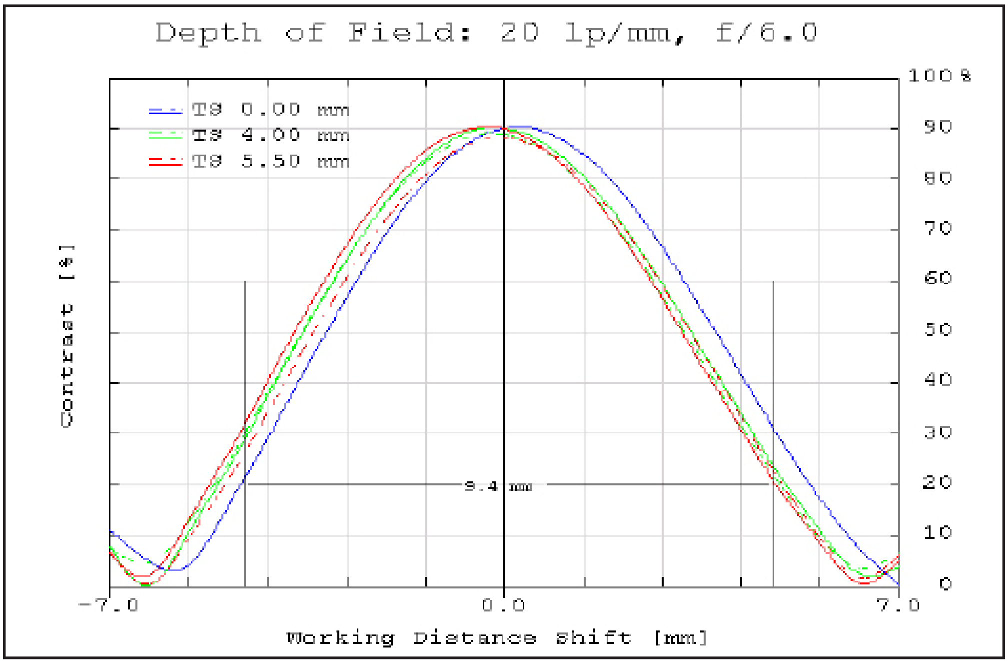

Figure 4: Polychromatic diffraction through-focus MTF at 20 linepairs/mm (image space). The depth of field at the maximum sensor format for the plotted frequency and f/# at 20% contrast is indicated by the measurement bars.

Plots represent theoretical values from lens design software. Actual lens performance varies due to manufacturing tolerances.

TECHSPEC® GOLD SERIES FOCUSABLE TELECENTRIC LENS

#55-349 • 161 - 186mm WD • 0.25X

MTF & DOF: f/10.0

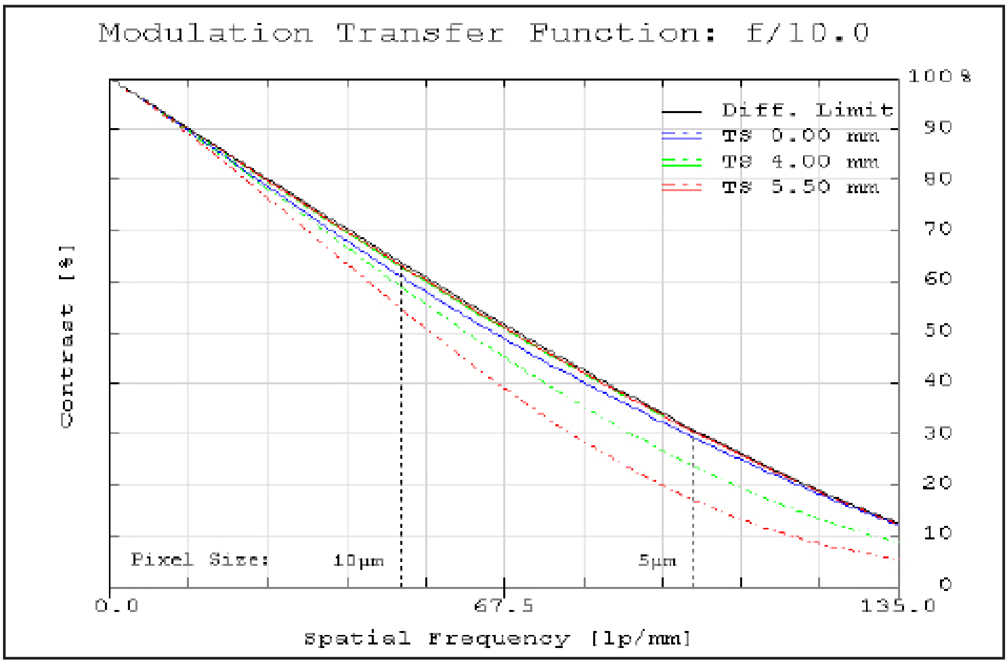

Figure 5: Image space polychromatic diffraction FFT Modulation Transfer Function (MTF) for λ = 486nm to 656nm. Included are Tangential and Sagittal values for field points on center, at 70% of full field and at the maximum sensor format. Solid black line indicates diffraction limit determined by f/#-defined aperture. Frequencies corresponding to the Nyquist resolution limit of pixel sizes are indicated.

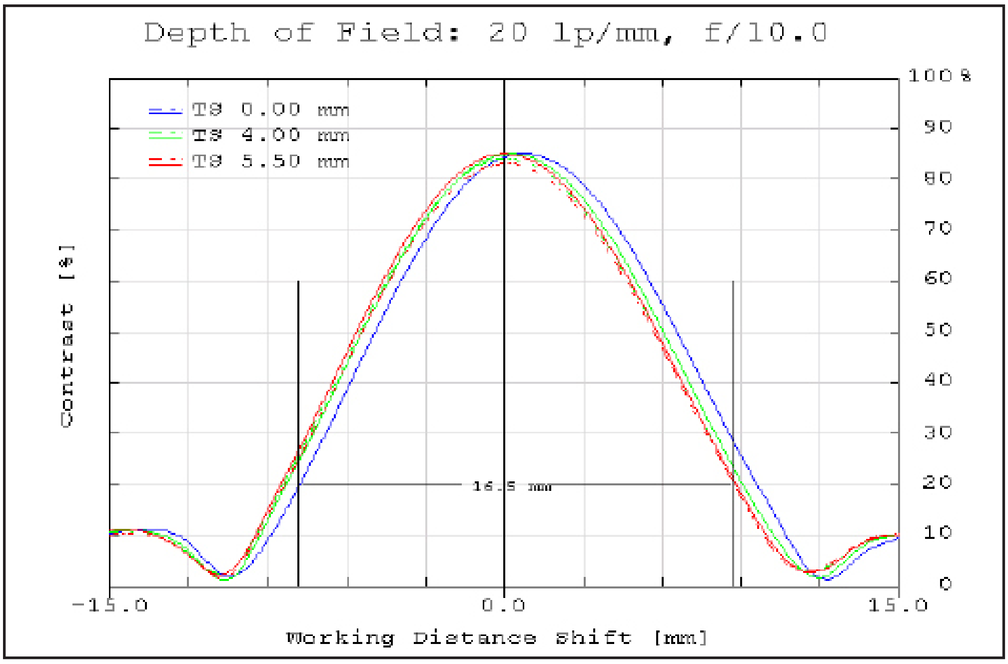

Figure 6: Polychromatic diffraction through-focus MTF at 20 linepairs/mm (image space). The depth of field at the maximum sensor format for the plotted frequency and f/# at 20% contrast is indicated by the measurement bars.

Plots represent theoretical values from lens design software. Actual lens performance varies due to manufacturing tolerances.

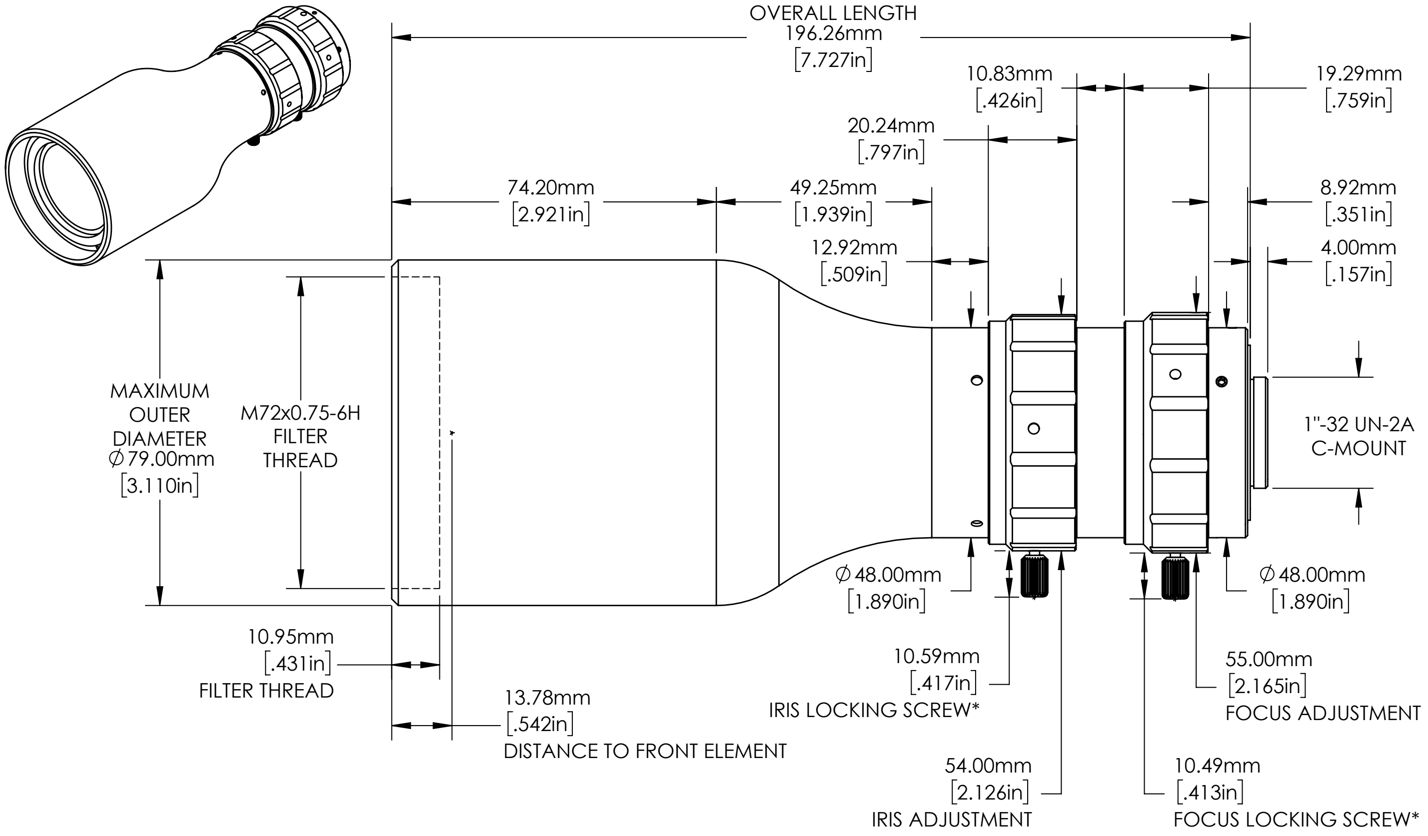

*ALSO INCLUDES RECESSED SET SCREW OPTION

FOR INFORMATION ONLY:
DO NOT MANUFACTURE PARTS TO THIS DRAWING

SPECIFICATIONS SUBJECT TO CHANGE WITHOUT NOTICE.
DIMENSIONS ARE FOR REFERENCE ONLY.
FOR DETAILED SPECIFICATIONS, PLEASE REFER TO THE SPEC SHEET.

Edmund Optics®

TITLE	0.25X 2/3" GoldTL™ Telecentric Lens	
DWG NO	55349	SHEET 1 OF 1

ETH
Eidgenössische Technische Hochschule Zürich
Swiss Federal Institute of Technology Zurich

Declaration of originality

The signed declaration of originality is a component of every semester paper, Bachelor's thesis, Master's thesis and any other degree paper undertaken during the course of studies, including the respective electronic versions.

Lecturers may also require a declaration of originality for other written papers compiled for their courses.

I hereby confirm that I am the sole author of the written work here enclosed and that I have compiled it in my own words. Parts excepted are corrections of form and content by the supervisor.

Title of work (in block letters):

Deformation Analysis and Finite Element Modelling for Ti-6Al-4V Additive Manufactured Lattices

Authored by (in block letters):
For papers written by groups the names of all authors are required.

Name(s):	**First name(s):**
Robmann	Serjosha

With my signature I confirm that

- I have committed none of the forms of plagiarism described in the 'Citation etiquette' information sheet.
- I have documented all methods, data and processes truthfully.
- I have not manipulated any data.
- I have mentioned all persons who were significant facilitators of the work.

I am aware that the work may be screened electronically for plagiarism.

Place, date	**Signature(s)**
Volketswil, 30.08.2019	

For papers written by groups the names of all authors are required. Their signatures collectively guarantee the entire content of the written paper.